Spectroscopy of a tetrahedral doubly magic candidate nucleus ^{160}_70**Yb**_90

A. Saha, T. Bhattacharjee, D. Curien, J. Dudek, I. Dedes, K. Mazurek, A. Góźdź, S. Tagami, Y.R. Shimizu, S.R. Banerjee, et al.

To cite this version:

A. Saha, T. Bhattacharjee, D. Curien, J. Dudek, I. Dedes, et al.. Spectroscopy of a tetrahedral doubly magic candidate nucleus ^{160}_70Yb_90. Journal of Physics G: Nuclear and Particle Physics, 2019, 46 (5), pp.055102. ⟨10.1088/1361-6471/ab0573⟩. ⟨hal-02097255⟩

HAL Id: hal-02097255
https://hal.science/hal-02097255v1

Submitted on 2 Sep 2020

Spectroscopy of a tetrahedral doubly magic candidate nucleus $^{160}_{70}\mathrm{Yb}_{90}$

A Saha[1,2]‡, T Bhattacharjee[1,2]§, D Curien[3], J Dudek[3,4], I Dedes[4], K Mazurek[5], A Góźdź[4], S Tagami[6], Y R Shimizu[6], S R Banerjee[1,2], S Rajbanshi[7]‖, A Bisoi[7]¶, G De Angelis[8], Soumik Bhattacharya[1,2], S Bhattacharyya[1,2], S Biswas[9], A Chakraborty[10+], S Das Gupta[1*], B Dey[1,2]♯, A Goswami[7], D Mondal[1,2], D Pandit[1,2], R Palit[9], T Roy[1,2], R P Singh[11], M Saha Sarkar[7], S Saha[9], J Sethi[9]

[1]Variable Energy Cyclotron Centre, IN-700 064 Kolkata, India
[2]Homi Bhabha National Institute, Training School Complex, Anushakti Nagar, IN-400 094 Mumbai, India
[3]Université de Strasbourg, CNRS, IPHC UMR 7178, F-67000 Strasbourg, France
[4]Institute of Physics, Marie Curie-Skłodowska University, PL-20 031 Lublin, Poland
[5]The Niewodniczański Institute of Nuclear Physics, Polish Academy of Sciences, 2 ul. Radzikowskiego 152, PL-31 342 Kraków, Poland
[6]Department of Physics, Faculty of Sciences, Kyushu University, Fukuoka JP-819 0359, Japan
[7]Saha Institute of Nuclear Physics, IN-700 064 Kolkata, India
[8]INFN, Laboratori Nazionali di Legnaro, IT-35 020 Legnaro, Italy
[9]Tata Institute of Fundamental Research, IN-400 005 Mumbai, India
[10]Department of Physics, Krishnath College, IN-742 101 West Bengal, India
[11]Inter University Accelerator Centre, IN-110 067 New Delhi, India

E-mail: `btumpa@vecc.gov.in`

Received

Abstract. The decay scheme of ^{160}Yb nucleus populated in the ^{148}Sm(^{16}O, 4n)^{160}Yb reaction at 90 MeV has been studied. The gamma-coincidence data have been collected by using Indian National Gamma Array (INGA) composed of twenty Compton-suppressed Clover-Germanium detectors. Compared to the prior publications, the

---

‡ Present Address: Physics Department, Indian Institute of Technology Bombay, Powai, IN-400 076 Mumbai, India
§ Corresponding Author
‖ Present Address: Dum Dum Motijheel College; 1, Motijheel Avenue; Dum Dum; IN-700 074 Kolkata, India
¶ Present Address:Indian Institute of Engineering Science and Technology, Shibpur, IN-711 103 West Bengal, India
+ Present Address: Siksha Bhavana, Visva-Bharati, Santiniketan 731 235, West Bengal, India
* Present Address: Victoria Institution (College), 78 B, A. P. C. Road, IN-700 009 Kolkata, India
♯ Present Address: Saha Institute of Nuclear Physics, IN-700 064 Kolkata, India

level scheme has been significantly modified owing to the observation of triple γ-coincidences and the measurements of γ intensities, R_θ (asymmetry ratio), DCO (Directional Correlation of Oriented States) and IPDCO (Integrated Polarisation Directional Correlation of Oriented States) ratios.

Theoretical results relevant for the exotic shape-coexistence related to the present context are presented and discussed. They illustrate the consequences of the fact that ^{160}Yb is expected to be a doubly-magic (Z=70 and N=90) tetrahedral-symmetry nucleus as predicted by other authors. The historical criteria of identification of such a symmetry in nuclei are critically revisited in the context of the actual measurement and interpretation of its results and the precise new criteria are formulated employing recent results of the Fukuoka-Strasbourg collaboration.

The experimental results are interpreted and discussed in detail. Limiting values of branching ratios for transitions observed by other authors but unseen in the present work are estimated. The population criteria of the β and γ vibration bands are revisited and discussed.

Although no indication of the presence of the stable tetrahedral configuration has been obtained, arguments are given towards the possible presence of the Y_{32} ('tetrahedral component') vibrations around the ground-state equilibrium. With the improvement of the spectroscopic information provided by the new data the way is opened for designed experiment(s) based on the unambiguous identification criteria of tetrahedral symmetry presented in this article.

PACS numbers: 21.10.-k; 23.20.Lv; 29.40.Wk; 21.60.-n

1. Introduction

Quantum behaviour of atomic nuclei results from the underlying properties of many-body nuclear interactions, the latter known to be among the most complex in nature. The nucleon-nucleon interactions are non-central, non-local and may change the character from attractive to repulsive or vice versa, depending on the quantum states and the energy of the interacting particles. The associated many-body nuclear Hamiltonians are scalar – therefore invariant under rotations of the coordinate frames – and *a priori* one may expect that the spherical symmetry of the resulting nuclear objects is privileged.

This is not the case.

The great majority of nuclei known experimentally are non-spherical. The fact that one may speak about their 'deformation' and, more generally, about 'geometrical properties' of atomic nuclei, is a consequence of the mechanism referred to as *spontaneous symmetry breaking*. The latter, together with the short range of the nuclear interactions comparable with the nucleon sizes, makes it possible to introduce the notion of the *nuclear surfaces*. The symmetry properties of the latter can be identified with those of the nuclei themselves.

According to [1], Z=70 proton number and N=90 neutron number are the tetrahedral-symmetry magic-numbers so that $^{160}_{70}\text{Yb}_{90}$ is expected to produce big shell-gaps and possibly acquire equilibrium deformations at the non-vanishing (tetrahedral) deformation α_{32}. The possible existence of tetrahedral symmetry in subatomic physics, cf. [1, 2] and references therein, attracted attention of many authors because of the exotic nuclear structure elements implied by such symmetry:

- The pure tetrahedral nuclear configurations, once populated, are expected to act as nuclear 'black holes': The corresponding nuclei emit neither E1 nor E2 radiation and are expected to have lifetimes orders of magnitude longer than the quadrupole-deformed ground-states of the same nuclei. This mechanism may have primordial consequences for the studies of the *exotic* nuclei, since those long-living tetrahedral configurations might offer the only chance of observing certain nuclei in laboratory.

- Tetrahedral symmetry is expected to imply non-negligible consequences for nucleosynthesis, because of the particularly long lifetimes of nuclei with this symmetry which are expected to provoke the existence of new waiting point nuclei.

- Tetrahedral symmetry has important new implications in nuclear spectroscopy because of the presence of four-fold degenerate nucleonic levels (thus 16-fold degenerate particle-hole excitations), totally new spectroscopic selection rules and many others.

Interested reader may consult the recent article [3] in which the first discovery of the combined tetrahedral and octahedral symmetries in a rare earth nucleus ^{152}Sm was announced. The present authors attempted searching for the similar evidence of the tetrahedral symmetry in ^{160}Yb, but did not succeed. This can be the result of insufficient instrumental sensitivity, but also restrictive impact of other conditions necessary for the experimental identification discussed in detail in [3]. Given growing interest in establishing the exotic tetrahedral and octahedral symmetries in subatomic physics, new experimental efforts will be needed in particular in ^{160}Yb with as unambiguous information about its energy spectrum as possible.

Yet, over 70 transitions in the studied decay scheme out of nearly 180, cf. [4, 5], are *not* confirmed by our experiment, even though our instrumental efficiency was enhanced compared to those used previously. In particular, we were able to perform a triple γ-coincidence analysis [not the case of the mentioned other publications] discussed in detail in section 5. We have demonstrated that many possibly incorrect attributions are correlated with the presence of doublets and triplets in the spectra. The absence of the mentioned transitions can be affirmed at the level of 0.1% of the strongest transition under the conditions of the present experiment.

We believe that the existence in the literature of a most probably flawed level scheme for this particularly important nucleus may considerably hamper the new research efforts aiming at the identification of the tetrahedral symmetry in the tetrahedral doubly-magic ^{160}Yb – especially since the electromagnetic transitions carrying possibly some information related to the symmetries in question are expected to be very weak. Moreover, the so-called 'three-band mixing' and 'four-band mixing' calculations reported in [4], has lead the authors of the cited article to the conclusion that their tetrahedral-symmetry candidate-bands in ^{160}Yb must not carry tetrahedral symmetry. Since these authors used a number of rather questionable transitions and levels, their discussion will need to be re-visited – even though this does not imply at all that the bands in question may carry signals of high-rank symmetries. From the arguments published e.g. in [3], cf. also references therein, as well as from the schematic illustration in figure 6 and from the surrounding text it follows that the tetrahedral-symmetry bands are composed of both-parity states and contain doublets and other characteristic structures so that the bands mentioned in the cited reference are certainly not the tetrahedral-symmetry candidates.

In the present work, the spectroscopy of ^{160}Yb has been revisited in order to study the low and moderate spin structure of this nucleus by using conventional gamma ray spectroscopic technique with the Indian National Gamma Array (INGA). The nucleus ^{160}Yb has been populated by using the fusion evaporation reaction ^{148}Sm(^{16}O, 4n)^{160}Yb at E_{beam} = 90 MeV. The γ-transitions have been detected with twenty Compton suppressed Clover HPGe detectors and the level structure has been deduced from the measurements of double-, and triple γ-coincidences, relative intensities, DCO (Directional Correlation of Oriented States), R(θ) (asymmetry ratio) and IPDCO (Integrated Polarisation Directional Correlation of Oriented States), by using conventional techniques. The DCO, R(θ) and IPDCO ratios have been extracted for the first time in the present work for some of the transitions. Moreover, relative intensities of certain gamma transitions along with their DCO, R(θ) and IPDCO values have been obtained for the first time here.

Several fragments of the level scheme obtained in the present work differ considerably from the ones obtained in some earlier measurements – as discussed below. In particular, the quadrupole-to-dipole branching ratios, $B(E2)_{in}/B(E1)_{out}$, for the decay of the odd-, and even-spin negative-parity sequences (Band-5 and Band-6; cf. figure 9 and 10) have been extracted from the relative intensities of the relevant transitions showing significant differences as compared to the earlier publications related to this nucleus. The latter results have been compared with the analogous ones in the other Rare Earth nuclei in this mass region, showing trends similar to the ones obtained here for the odd and even-spin negative-parity sequences, as discussed in detail below.

The detailed description of the experiment itself, together with the data analysis, the selective power of the gamma array used and, finally, the obtained level scheme of ^{160}Yb are presented in section 5.

Given the fact that the precise group-theory based conditions of identification of the nuclear tetrahedral symmetry bands are known today, cf. [3], and references therein, it was not difficult to establish that none of the bands observed by us satisfies the sought tetrahedral-symmetry conditions. However the results of our modelling suggest that α_{32} shape oscillations of the prolate shape ground-state minimum may give rise to the negative-parity bands whose expected properties will be discussed in the article. Independently, several articles seeking the signs of the tetrahedral symmetry bands published in the past were based on the arguments of partial symmetry breaking – among others *via* quadrupole-shape zero-point motion around the tetrahedral-symmetry minima as well as via Coriolis coupling mechanism whose effects are expected to increase with increasing spin. Our critical comments related to those types of interpretations will be discussed as well.

2. Decay Scheme and Structure Studies of ^{160}Yb: The *Status Quo* Before This Experiment

The experimental investigation methods used to study the ^{160}Yb nucleus employed various techniques as well as various population pathways that range from decay spectroscopy to ultra high-spin spectroscopy c.f. [6, 7, 8] and [4, 5, 9, 10, 11, 12, 13, 14]. The primary information about the low-energy level-structure of this nucleus comes principally from two measurements of the decay of ^{160}Lu [9, 10]. Riedinger and collaborators have first observed four negative-parity bands in ^{160}Yb (cf. Band-2, Band-3, Band-4 and Band-5 in figure 10), which were interpreted in terms of two quasiparticle configurations originating from the $\nu \mathrm{i}_{\frac{13}{2}}$ and $\nu \mathrm{h}_{\frac{9}{2}}/\nu \mathrm{f}_{\frac{7}{2}}$ orbitals, cf. [7].

The first measurements of lifetimes of certain levels in the negative-parity Band-3 and Band-4 have been performed by Fewell *et al.*, [11, 12], using RDM technique. The authors of the latter work found out that the transition quadrupole-moments of these bands are similar to that of the yrast band. They also found a similar frequency-dependent reduction of the quadrupole moments with increasing spin. From the latter observation they conjectured that Band-3 and Band-4 contain the contribution from the aligning $\mathrm{i}_{13/2}$-orbital. Such similarities support the suggestion that Band-3 and Band-4 are signature partners [6, 7]. In the latter work, the shape evolution at high spins was suggested on the basis of the systematic deviation of the band energies from the usual $E_I \sim I(I+1)$ pattern.

It has also been found out that the odd-spin negative-parity Band-5 has a clearly distinct alignment behaviour as compared to the other negative-parity bands [7] what has led the authors to interpreting its distinct structure in terms of a distinct mechanism: pear-shape octupole-vibration. The negative-parity Bands-2, 3, 4, 5 and 6 have been also reported in [4].

The nucleus ^{160}Yb, has also been in the centre of attention in the very early stages of the development of the realistic microscopic mean-field methods – in particular their pairing self-consistent, the so-called Hartree-Fock-Bogolyubov Cranking (HFB-C) realisation. Indeed, one of the first microscopic calculations of this type using the HFB-C method [15] with the Woods-Saxon mean-field Hamiltonian and its so-called universal parameterisation (cf. [16] for the early references) was applied to ^{160}Yb nucleus. In [15], the freshly discovered at that time, the experimental ^{160}Yb *double back-bending* curves of [17], representing the kinematical moment of inertia, $J^{(1)}$ *vs.* rotational frequency, were reproduced with a surprising for those times an accuracy – and this, at the microscopically calculated equilibrium deformation, cf. figure 1 in [15]. The underlying mechanism, as discovered simultaneously, was the alignment of the high-j nucleon angular momenta at the spins around $I = 12\,\hbar$ in the case of the neutrons and at I in the vicinity of $28\,\hbar$ in the case of protons - thus giving rise to the double back-bending.

The theoretical method used in these early calculations was a realistic, microscopic, pairing self-consistent approach based on the earlier suggestions in [18] and [19]. These calculations were extended in [6] in terms of the spin range, reaching the $I = 50\,\hbar$ spin limits, and moreover, in terms of the precision addressing the variations of the second order derivatives of the energy *vs.* spin dependence, d^2E/dI^2, related to the so-called dynamical moments, $J^{(2)}$.

The underlying quasi-particle structures of the excited bands and the band crossing frequencies in ^{160}Yb were discussed in the early articles [7] and [8] whereas the systematic properties of the shape coexistence and evolution throughout the periodic table in [20]. Since then these techniques have been developed further and applied in numerous publications. The cranking-approximation has proven to be an important tool in the research of nuclear collective rotation and its interplay with the single-particle degrees of freedom in the presence of pairing.

As recalled in the preceding sections, one of the nuclear ranges in which the presence of the tetrahedral symmetry has been predicted in [1, 2], is centred at the tetrahedral magic gaps at Z = 70 and N = 90, corresponding to ^{160}Yb, the nucleus of principal interest in this article. These early tetrahedral-symmetry predictions have been supported as well by other theoretical calculations [21, 22]. However, the issue of the experimental signatures of such structures in medium heavy and heavy nuclei has been a subject of a number of qualitative arguments in many anterior publications and has been clarified only in the recent Fukuoka-Strasbourg collaboration articles, cf. [23, 24] – cf. also a qualitative illustration in figure 6 and surrounding text in the present article.

3. An Overview of the Shape-Coexistence Effects in ^{160}Yb

Here and in the following we refer to various types of nuclear shapes and their symmetries using the standard multipole expansion of the nuclear surface, say Σ, in terms of the basis of spherical harmonics $Y_{\lambda\mu}$:

$$\Sigma: \quad R(\vartheta,\varphi) = R_0\, c(\{\alpha\})\Big[1 + \sum_{\lambda}\sum_{\mu} \alpha^*_{\lambda\mu} Y_{\lambda\mu}(\vartheta,\varphi)\Big], \tag{1}$$

using the usual symbols and notation. Above, $R_0 = r_0 A^{1/3}$, with A representing the mass-number and $r_0 \approx 1.2\,\mathrm{fm}$, is usually called radius parameter. The nuclear surface expansion-coefficients, $\alpha_{\lambda\mu}$, are called multipole deformations or multipole deformation parameters, whereas $c(\{\alpha\})$ is an auxiliary function assuring that the nuclear volume does not depend on the actual shape of its surface. Here and in the following, the symbol $\{\alpha\} \equiv \{\alpha_{\lambda\mu}\}$ denotes the full set of all non-zero deformation parameters.

Calculations of the total energy surfaces using realistic microscopic mean-field theory methods have been focussing on the Rare Earth nuclei since the early days of the extensive studies of the super-deformation at high-spins, from the eighties onwards, and thus many examples of such calculations can be found in the literature. The results of the calculations obtained previously using the methods similar to those employed in the present study can be found e.g. in the early articles [6] and [20].

Let us emphasise that the discussion of the shape coexistence effects presented below is limited to the static, no-rotation case. Such a representation emphasises the role of the tetrahedral symmetry minima. Indeed, the rotation effects usually represented within the mean-field theories using the cranking approximation introduce explicitly the role of the Coriolis polarisation which is expected to break the tetrahedral symmetry by distinguishing the axis of rotation as a tetrahedral-symmetry breaking element.

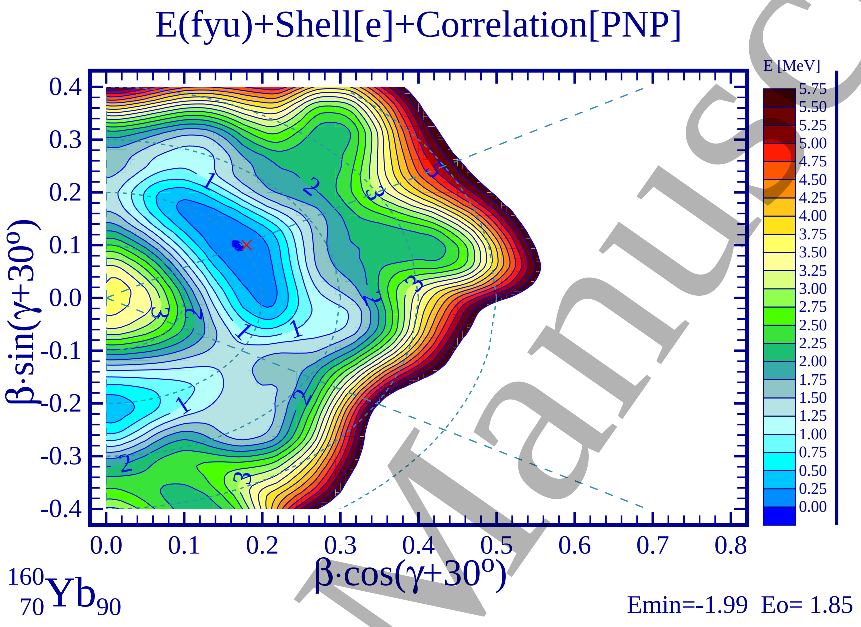

Figure 1. Nuclear potential energy surface corresponding to the ground-state configuration. Results obtained using the microscopic-macroscopic method with the deformed Woods-Saxon potential – cf. [16] and references therein and [20] – represented with the help of the traditional shape parameterisation using Bohr's parameters (β, γ).

For the sake of the following discussion, it will be instructive to consider first the two-dimensional (β, γ)-plane projection of the total energy of the ^{160}Yb nucleus, cf. figure 1. By definition, the β and γ parameters are related to the multipole expansion parameters of equation (1) through $\alpha_{20} = \beta \cos\gamma$ and $\alpha_{22} = \frac{1}{\sqrt{2}}\beta \sin\gamma$. At each (β, γ)-point the nuclear energy was minimised over the hexadecapole deformation α_{40} to make the predictions more realistic. The up-sloping axis corresponds by definition to the tri-axiality parameter $\gamma = 0$ and thus to the axially-symmetric prolate shapes. The vertical, $\gamma = 60^0$-axis corresponds to the axially-symmetric oblate shapes (so are the shapes related to the down-sloping $\gamma = -60^o$ straight line) whereas the down-sloping vertical axis describes again the prolate shapes of axial symmetry. Note that since at each (β, γ)-point the energy was minimised with respect to $\alpha_{40} \equiv \beta_4$, the otherwise well known symmetry in terms of the $(\Delta\gamma = 60^o)$-sectors is not exactly respected.

The corresponding diagram can be considered as a typical illustration of the nuclear potential energy surface as a function of both quadrupole deformations. As it can be seen form the figure, a pronounced, the so-called "γ-softness" (a flatness of the landscape in the γ-direction) is predicted, characteristic of the transitional character of the discussed nucleus, suggesting at the same time a possible presence of low-energy γ-vibrations.

However, as demonstrated in [1] and [2], the information of the type contained in figure 1, may easily turn out to be rather incomplete. Indeed, systematic calculations in the above cited articles have shown that when the space of the deformation parameters is sufficiently rich, compared to just quadrupole-deformation space, a new form of an exotic shape coexistence arises in certain nuclei such as ^{160}Yb. The nuclear energies corresponding to these new exotic minima are comparable to the energies at the ground-state minima as illustrated below.

3.1. Remarks about Exotic Symmetries and Realistic Mean-Field Theory Predictions

It will be worth reminding the reader that whereas tetrahedral symmetry has been observed abundantly in molecular physics, its observation in nuclear structure physics remains a challenge. From the mathematical point of view, the point group representing tetrahedral symmetry of geometrical surfaces, T_d, is composed of 24 symmetry elements. In the quantum mechanics of the fermion systems such as atomic nuclei, its so-called double point group partner, T_d^D, composed of 48 symmetry elements is applicable as an indicator of the tetrahedral symmetry of the corresponding Hamiltonian for nucleons. Moreover, tetrahedral group can be seen as a subgroup of the octahedral (O_h^D) point-group, $T_d^D \subset O_h^D$, the latter composed of 96 symmetry elements. The mean-field Hamiltonians symmetric with respect to any of these two groups produce the single-particle eigenvalues with four-fold degeneracies [recall at this point that the 'usual' Kramers degeneracies of all nucleon levels in the deformed (but not the discussed T_d^D-, or O_h^D-symmetric) potentials are two-fold].

Because of this four-fold degeneracy characteristic for the T_d^D-, and O_h^D-type symmetric Hamiltonians and unexpected otherwise, the T_d^D and O_h^D groups have been nicknamed *high-rank symmetries*. The so-called octahedral deformations have been introduced in [25], where the associated methods of nuclear energy minimisation have been discussed as well.

The realistic calculation results of the single nucleon levels show very strong shell effects at the non-zero tetrahedral deformations. As it turns out, the shell-gaps of the order of 2.0 - 2.5 MeV for Z/N=70 and about 3 MeV for N=90/94 have very strong impact on the calculated new type total energy minima, figure 2. The total energy projection on the plane of the quadrupole α_{20}-, and the tetrahedral α_{32}-deformation is illustrated in figure 2 showing the presence of two, symmetric, well pronounced total energy minima, in addition to the prolate ($\alpha_{20} \approx 0.2$) and the oblate ($\alpha_{20} \approx -0.2$) competing, so to speak 'traditional', quadrupole prolate-oblate shape minima. [It is worth emphasising that the oblate-shape minimum in this particular nucleus is, what is called, 'γ-unstable', cf. figure 1 and related discussion.]

Let us emphasise that the tetrahedral symmetry minima at $\alpha_{32} \approx \pm 0.18$ and $\alpha_{20} \approx 0$ in figure 2 correspond to the energies *comparable* to the energy of the

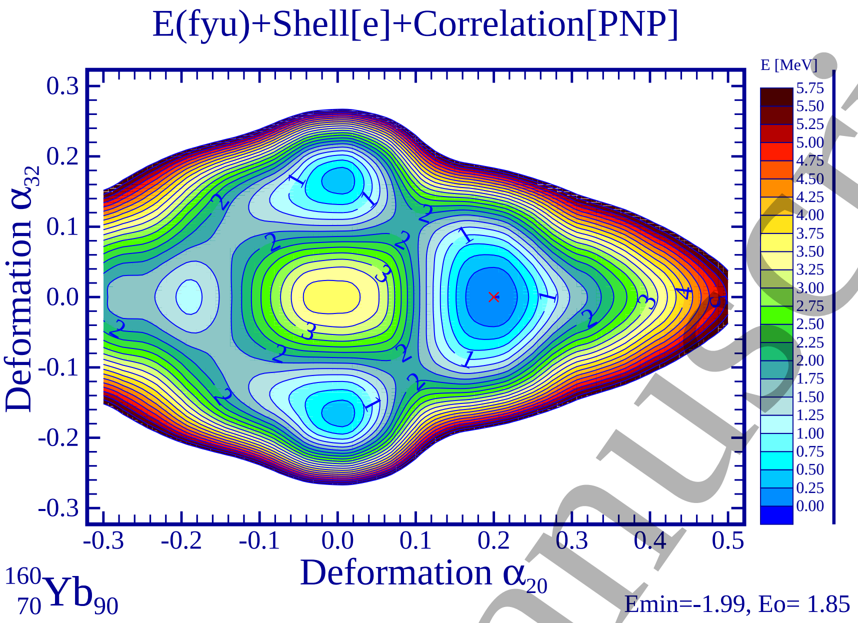

Figure 2. The total energy $(\alpha_{20}, \alpha_{32})$-plane projection calculated using the same microscopic-macroscopic method and the deformed Woods-Saxon potential, as the one discussed in the context of figure 1. The two symmetric minima at $\alpha_{32} = \pm 0.18$ represent the exotic shape coexisting configurations carrying tetrahedral symmetry. At each deformation point the energy was minimised over the octahedral deformation of the first order, o_4; for its definition and the motivations of the use in the present context, see [25]. As for the prolate-oblate shape coexistence (visible in this figure but absent in figure 1) see also comments in sections 3.1 and 3.2.

ground state. These results have been obtained using the same theoretical method (macroscopic-microscopic method with the Yukawa-folded macroscopic term of [26] and the deformed Woods-Saxon potential with its 'universal' parameterisation of [16]) which have been successfully used to describe among others the octupole effects in the early articles [27, 28, 29, 30]. Since this research was successfully followed up to date by independent groups of physicists working on various similar applications, we may believe in the predictive power and stability of the underlying method.

It will be instructive to compare the results presented in figure 2 (recall that the deformation α_{32} is sometimes referred to as 'triaxial octupole deformation') with similar results in which α_{32} is replaced by α_{30}, the 'traditional' pear-shape octupole axial-symmetry deformation. The corresponding two-dimensional projections of the total energy on the plane $(\alpha_{20}, \alpha_{30})$ are presented in figure 3. Comparison of the last two figures indicates that the pear-shape *oscillations* around the quadrupole-deformed ground-state minimum might be energetically privileged since the stiffness against these pear-shape oscillation is much weaker (the energy landscape much flatter) in the direction of the α_{30}-axis as compared to that along the α_{32}-axis, as seen from comparison

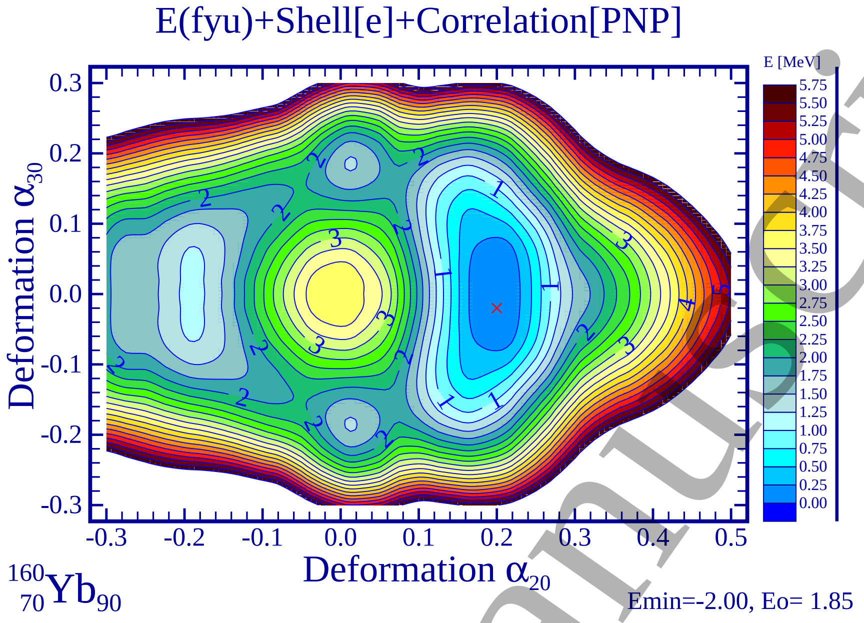

Figure 3. The total energy results obtained using the same microscopic-macroscopic method with the deformed universal Woods-Saxon potential as in the case of the illustrations in figures 1 and 2. At each $(\alpha_{20}, \alpha_{30})$-point the energy was minimised over the hexadecapole deformation α_{40}, to obtain a more realistic estimate, cf. figure 1. Let us notice the presence of the 'traditional' prolate-oblate shape minima at $\alpha_{20} \approx \pm 0.2$ (see comments in section 3.2) and the presence of two shallow symmetric minima at $\alpha_{30} \approx \pm 0.2$. The geometry of the latter ones can be described as that of a superposition of the left-right asymmetric pear-shapes with the surface of the sphere. The barriers surrounding the two octupole minima are, nevertheless, very likely too low to lead to associated measurable effects.

of the figures 2 and 3; we return to these issues later in this article.

3.2. Comments about Shape Coexistence in Terms of Octupole Deformations

The special role of the low-lying tetrahedral energy minima in ^{160}Yb has already been emphasised and possible competition with the pear-shape configurations mentioned. Since the pear-shape octupole deformations are predicted to give rise to a flatness of the nuclear energy landscape in the α_{30}-direction in the vicinity of the quadrupole-equilibrium, it is natural to examine a possible competition between these two degrees of freedom. The possible presence of the pear-shape octupole components is important in the present context since it may contribute to the E1-transitions otherwise forbidden by the tetrahedral symmetry.

The corresponding results for the potential energy are illustrated in the form of the $(\alpha_{30}, \alpha_{32})$-plane projection in figure 4. The $(\alpha_{30}, \alpha_{32})$-representation is analogous to the one in figure 1, where the projection on the $(\alpha_{20}, \alpha_{22})$-plane was shown. As it can be

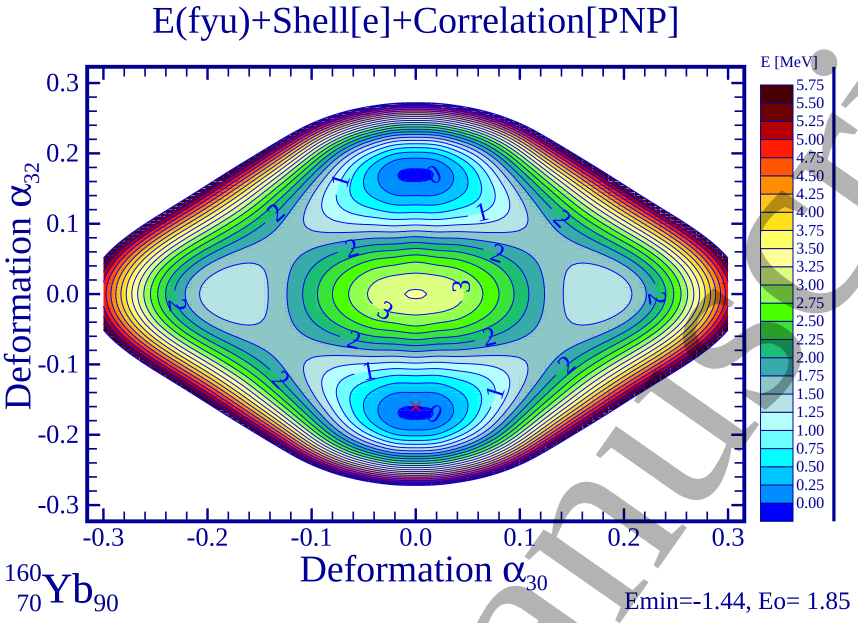

Figure 4. The total energy projection onto the $(\alpha_{30}, \alpha_{32})$-plane. Since this illustration aims at presenting the competition between the octupole minima in figures 2 and 3, both corresponding to $\alpha_{20} \approx 0$, this latter quadrupole deformation was set to zero in this particular illustration. As it can be seen from the figure, the tetrahedral minima with $\alpha_{32} \approx \pm 0.18$ lie approximately 1.5 MeV lower than the competing shallow pear-shape minima with $\alpha_{30} \approx \pm 0.18$.

seen from the figure, the tetrahedral symmetry minima clearly gain the competition.

It turns out that all other possible combinations of the $(\alpha_{3\mu}, \alpha_{3\mu'})$-projections (not shown) confirm the actual conclusions that the tetrahedral minima in ^{160}Yb are stable and can be considered as firm predictions obtained within the realistic microscopic mean-field theory. Comparison of the behaviour of the potential energy surfaces close to the axially-symmetric quadrupole energy minima indicates the characteristic behaviour as far as the projections onto the orthogonal axes $\alpha_{3\mu} \perp \alpha_{20}$ are concerned: A dominating flatness in the direction of the α_{30}-axis, as compared to the other 'octupole directions'. This implies that the $K^\pi = 0^-$ collective octupole vibration excited-states may lie relatively lower as compared to the $(K > 0)^-$ collective vibrations with the analogous implications for the positions of the band-heads and the rotational band structures.

Some specific consequences of these observations pertinent for the ^{160}Yb nucleus will be discussed below.

4. Tetrahedral Symmetry: Historical vs. Most Recent Search Scenarios

The question of identifying for the first time the existence of nuclear states with tetrahedral symmetry in medium-heavy and heavy nuclei has preoccupied physicists participating in this type of research in the recent years, see e.g. [31] for an overview of the progress in the years which followed the predictions in [1]. From the today's perspective it can be observed, that the problem of a distinction between the necessary and the sufficient conditions, which would allow for an unambiguous detection of the tetrahedral symmetry has lead to a certain confusion in the past. Therefore, it will be instructive at this point to discuss these issues briefly.

4.1. Hypothetical Identification of the Tetrahedral Symmetry States via *Partial Symmetry Breaking*

According to the collective model, these are not so much the *static equilibrium* points at the potential-energy minima, which determine the effective physical deformation of the system, but rather the most probable deformations calculated according to the rules of quantum mechanics with the help of the collective wave functions. These wave functions take into account the zero-point motion and/or the structure of the lowest-lying e.g. one-phonon excited-state wave-functions. Inspection of the results in figure 2 shows that such oscillations around the tetrahedral minimum in the direction of the α_{20}-axis, the latter orthogonal with respect to the α_{32} 'tetrahedral' axis, may indeed lead to some – even if small – induced, effective (or 'residual') quadrupole moments. Similar observation can be made in relation to the induced dipole moments associated with the pear-shape oscillations along the α_{30}-axis orthogonal with respect to the other two, as can be deduced from figure 4. Moreover, the pear-shape oscillations, even around the zero quadrupole deformation equilibrium point, generate non-zero quadrupole moments as can be shown analytically. Similarly the residual dipole moments are induced under the discussed conditions. It is a matter of the actual values of the stiffness of the potential energy and non-trivial collective model calculations including the microscopic determination of the mass tensor to determine how small are in reality the 'residual' dipole and quadrupole moments induced dynamically via collective oscillations.

Moreover, the collective angular momentum vector defines an extra direction in space thus breaking the initial tetrahedral symmetry of the mean-field Hamiltonian invariant under 48 symmetry elements at null rotation. One should expect that the higher the collective angular momentum, the stronger the breaking of the tetrahedral symmetry via Coriolis coupling and thus the chances of inducing the non-zero quadrupole and dipole moments helping to populate or de-excite the high-rank symmetry states *via* 'residual' E1 or E2 electromagnetic transitions.

We thus arrive at a possibility of formulating the following conjecture: Due to the presence of the discussed residual dipole and quadrupole collective moments, the relatively high-spin states corresponding to the tetrahedral minima could in principle be populated via, possibly weak, E1 or E2 transitions. Under such an *assumption*, at sufficiently high spins both the quadrupole and dipole moments will not exactly vanish, even if remaining relatively small and, *in principle*, an existence of both the E2 intra-band transitions and the E1 inter-band transitions, the latter ones de-exciting the negative-parity bands to a positive-parity e.g. ground-state band, might not be *a priori* excluded. These effects may be even strengthened by the presence of extra particles or holes on top of the tetrahedral magic closures.

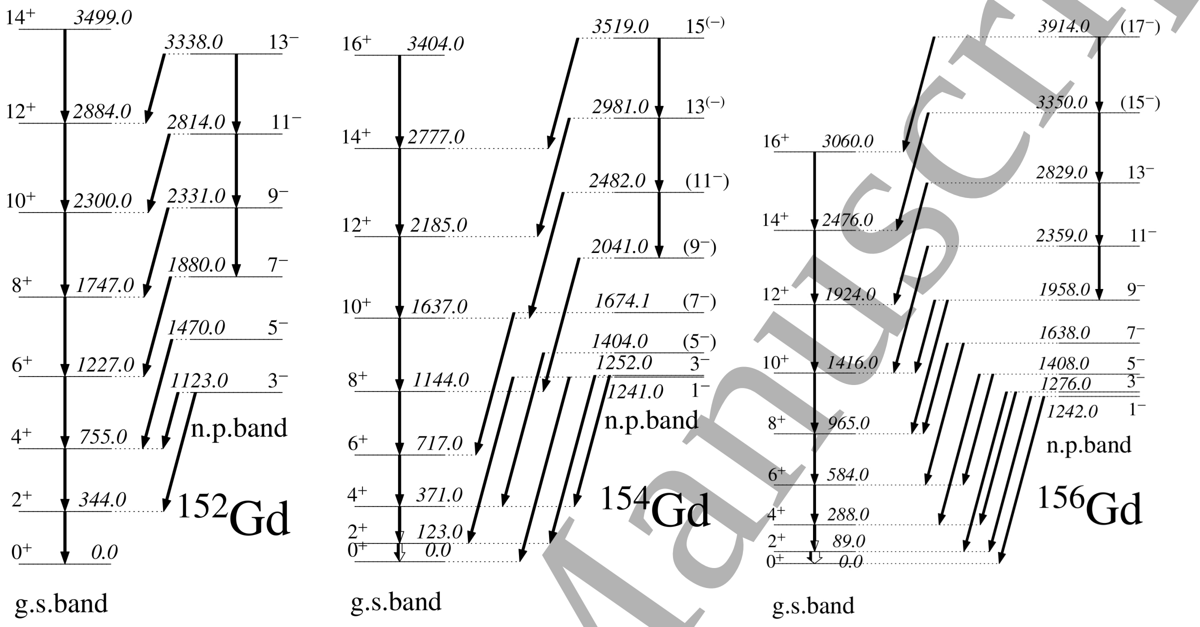

Figure 5. Examples of the odd-spin negative-parity bands in three Gadolinium nuclei (proton number Z=64 can be considered as a magic-tetrahedral particle number) with the neutron numbers N=88, 90 and 92 (neutron number N=90 is the another magic-tetrahedral particle-number). Note that the E2 intra-band transitions were too weak to be observed below certain spins, and the presence of the rotational bands was deduced via the measured E1 transitions. Experimental results are from http://www.nndc.bnl.gov/ensdf/ .

Let us *assume*, as a working hypothesis, that a negative-parity rotational band associated with the tetrahedral symmetry minimum has been populated at sufficiently high spins due to the presence of the residual dipole and quadrupole moments – thus under the conditions of a sufficiently strong breaking of the original symmetry. According to this 'historical scenario' advocated in the past, the residual Q_2-, and Q_1-moments result from the presence of the relatively high collective angular momenta breaking relatively strongly the tetrahedral symmetry via Coriolis coupling between the individual angular momenta $\hat{\jmath}$ and the total collective rotation angular momentum operator $\hat{R}$. However, with the spin decreasing along the band, the symmetry breaking decreases – so are the residual dipole and quadrupole moments.

The results presented in figure 5 are compatible with the decreasing of the reduced transition-probability ratio B(E2)/B(E1):

$$B(E2; I \to I-2)/B(E1; I \to I-1) \xrightarrow{I\to 0} 0, \qquad (2)$$

as expected from the vanishing Q_2 moments. However such a compatibility can be seen as merely a necessary condition: Should $Q_2 \to 0$ the relation in eq. (2) would follow, the inverse is not true. Indeed, let us notice that the $E2$ transition energies, $\Delta E_{\gamma-\mathrm{E2}}$, decrease approximately linearly with decreasing spin as it can be seen from figure 5, whereas the inter-band dipole transition energies, $\Delta E_{\gamma-\mathrm{E1}}$, do not change much with spin. [At this point it is *not* our intention to refer to the most recent data but rather present the results which have led in the past to the formulation of certain 'historical' necessary but not sufficient criteria of identifying tetrahedral symmetry.] It then follows that vanishing of the E2 transitions at the bottoms of the bands is compatible as well with the decreasing the ratios of probability, $P(E\lambda) \propto B(E\lambda) \cdot (\Delta E_{\gamma-E\lambda})^{(2\lambda+1)}$:

$$P(E2; I \to I-2)/P(E1; I \to I-1) \xrightarrow{I \to 0} 0, \tag{3}$$

the latter containing the transition energy factors proportional to $(\Delta E_{\gamma-\mathrm{E2}})^5$ and inversely proportional to $(\Delta E_{\gamma-\mathrm{E1}})^3$. Thus the discussed evolution could *not* be interpreted as a result the quadrupole moment approaching zero; the latter conclusion can be drawn exclusively from the direct measurement of the quadrupole moment in question. Such a measurement has been performed in [32] for ^{156}Gd nucleus showing that the quadrupole moment associated with the negative parity band in question is comparable to the ground-state quadrupole moment so that the disappearance of the $E2$-transitions (at least in the ^{156}Gd of figure 5) is not due to decreasing of the quadrupole moment.

It turns out that the just described scenario is found in several nuclei with the proton and neutron numbers close to the tetrahedral magic numbers both in the Rare Earth and Actinide nuclei. A few examples are shown in figure 5, in relation to the tetrahedral magic numbers Z=64 and N=90. It can be seen from the figure that the rotational sequences $E_I \propto I(I+1)$ are observed towards the bottoms of those negative-parity bands exclusively thanks to the E1-inter-band transitions. Similar patterns have been observed in the nuclei with the proton numbers between the Z=64 and Z=70: $^{152}_{62}\mathrm{Sm}_{90}$, $^{154}_{62}\mathrm{Sm}_{92}$, as well as in $^{154}_{66}\mathrm{Dy}_{88}$, $^{156}_{66}\mathrm{Dy}_{90}$ and $^{160}_{66}\mathrm{Dy}_{94}$ and $^{164}_{68}\mathrm{Er}_{96}$.

Analysing the experimental results in the present measurement we were not able to attribute the behaviour of branching ratios compatible with the discussed 'historical scenario' together with the verification of the condition of the associated quadruple moments approaching zero. It follows that none of the bands discussed in the present article can be interpreted as 'tetrahedral band according to historical criteria'.

4.2. Contemporary ideas about identification of the Tetrahedral Symmetry: Scenarios Guided by Group-Theory Considerations

In nuclear structure physics the term *rotational bands* is applied almost exclusively to 'sequences composed of levels with the energies $E_I \propto I(I+1)$, characterised either only by even or only by odd spins'. In molecular physics, where a rich collection of geometrical symmetries has been studied over the long time, it has been established that certain symmetry groups of the molecular Hamiltonians impose different selection rules.

In the context of the tetrahedral symmetry considerations, these selection rules have been re-visited recently within the Fukuoka-Strasbourg collaboration [23, 24, 3], for medium-heavy/heavy nuclei, using the state-of-the-art realistic spin-and-parity projection realisation of the mean-field theory. These calculations fully confirmed that due to the symmetry arguments derived rigorously from the theory of representations of groups (cf. e.g. appendix section of [23]), the irreducible representation associated with the lowest energy $E_I - vs. - I$ tetrahedral symmetry solutions allows for the precisely restricted spin sequences:

$$I^\pi = 0^+, 3^-, 4^+, 6^\pm, 7^-, 8^+, 9^\pm, 10^\pm, 11^-, 12_d^+, 12^- \ldots \tag{4}$$

Above, the subscript 'd' signifies a doublet of expected degenerate positive-parity $I = 12\,\hbar$ states, whereas the superscripts '±' indicate the presence of degenerate opposite-parity states (which in the realistic nuclear context may appear as close-lying) with the indicated spins. One should stress that the strict degeneracies apply to the exact symmetry limit, whereas in the realistic nuclear conditions various types of polarisation/perturbations may lead to near-degeneracy only.

Certain features of this exotic sequence, which we refer to as strict-symmetry tetrahedral band, are illustrated in figure 6 and deserve emphasising. Firstly, the tetrahedral symmetry imposes that the sequence in question contains two characteristic sub-sequences of opposite parities forming a common $E_I \propto I(I+1)$ parabola. These tetrahedral-octupole-rotational properties are distinctly at variance with the properties of rotational bands built on top of the octupole-pear-shape symmetry configurations. The latter contain the regular opposite-parity sequences with two parabolic $E_I \propto I(I+1)$ energy sequences with generally (even if only slightly) different moments of inertia – possibly manifesting parity doublets.

The single tetrahedral-band sequence in figure 6 should *not* be confused with a collection of separate positive and/or negative parity bands. For instance, the positive-parity $\Delta I = 2$ sequence beginning at $I^\pi = 4^+$, in contrast to certain tempting analogies followed in the literature, cannot be classified e.g. as $K^\pi = 4^+$ band, simply because it is an element of the more complex, tetrahedral band. This positive parity (sub)-sequence contains even spins (4, 6, 8, 10 ...) and occasionally odd-spins – in the considered spin range this is an $I^\pi = 9^+$ state as seen in figure 6.

Another, perhaps a surprising element on the list of exotic features, is the total absence of the $I^\pi = 4^-$ and 5^- states in the negative-parity sub-sequence of the discussed family – and the presence of the $\Delta I = 3$ band-members with spins $I^\pi = 3^-, 6^-, 9^-, \ldots$ as seen in the figure. The latter sequence is interrupted by the 'occasional' presence of other negative parity states ($I^\pi = 7^-$ or 10^-) as in the illustrated spin interval.

Finally one should emphasise another important feature of the discussed sequence: The energy-dependence of the states belonging to the tetrahedral-band in question is to an approximation parabolic at least within the spin-range considered for all the states listed. For the modelling whose results are represented in figure 6 we took the tetrahedral deformation of $\alpha_{32} \approx 0.18$, what corresponds to the result of the microscopic predictions

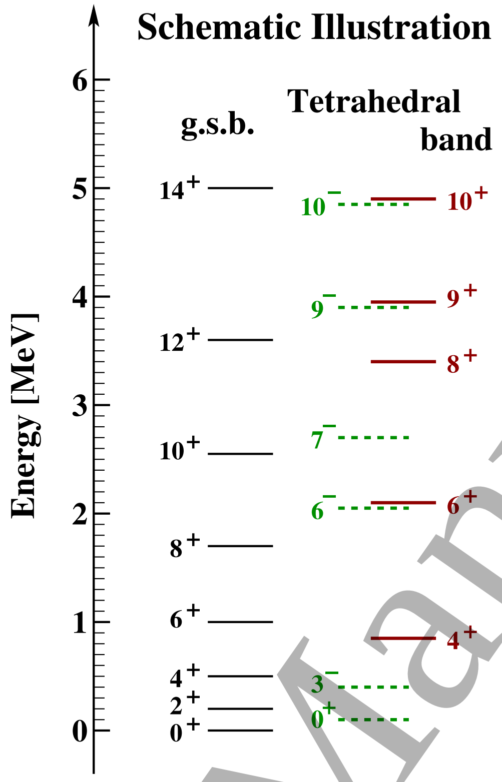

Figure 6. Theory predictions related to the properties of the lowest energy rotational band built on the tetrahedral-symmetry minimum (schematic illustration). The absence of states with certain spin-parity combinations deserves noticing as much as the fact that the energies of all the states shown form to a good approximation a common parabola which determines at the same time the effective moment of inertia of the band. The symbol g.s.b. refers to the ground-state band. In the exact symmetry limit the levels with $I^\pi = 6^\pm$, $9^\pm$, $10^\pm$ form degenerate doublets, cf. equation (4). Combination of these features is a unique consequence of the tetrahedral symmetry and can thus be used for an unambiguous experimental identification of tetrahedral symmetry in this nucleus in the future experiments.

in section 3.

We will not be able to present an evidence of the above characteristic tetrahedral-band decay pattern in this article – such a structure has not been observed in the present experiment – see however the results for ^{152}Sm in [3]. Its absence in our spectra is probably due to the expected weak population of the tetrahedral symmetry states in the present experiment. Recall: As mentioned on various occasions earlier in this article, the (nearly) vanishing dipole and quadrupole moments hinder the population of the tetrahedral symmetry states via the corresponding, usually enhanced E2 and E1 transitions accompanying heavy-ion x-n reactions. However, we will be able to present several new results in a semi-quantitative agreement with the expectations based on our theoretical modelling.

5. Experiment

The excited states in the ^{160}Yb nucleus were populated by using the HI fusion evaporation reaction ^{148}Sm(^{16}O, 4n)^{160}Yb with E_{beam} = 90 MeV from the 14UD Pelletron at TIFR, Mumbai. The 900 μg/cm^2 thick Sm_2O_3 target, 97% enriched and electro-deposited on a 3 mg/cm^2 Pb backing foil, was used in the experiment. The Indian National Gamma Array (INGA), consisting of twenty Compton suppressed Clover detectors at the time of experiment, was used for the detection of the γ-transitions. The detectors were arranged in seven rings around the target having angular positions of 23°, 40°, 65°, 90°, 115°, 140° and 157° with respect to the beam direction. Three detectors were kept in each of the rings except at 90° and 23°; in these two rings, there were four-, and one detector, respectively. A PCI-PXI based digital data acquisition system was used for the collection of two and higher fold time stamped data in list mode. Individual Pixie cards, each of which can accommodate four Clover signals, vetoed externally by individual BGO detector, were used for this purpose. The details of the data collection, sorting and analysis procedure are described in [33].

5.1. Data Analysis and Results

The obtained data have been sorted offline using the MARCOS (Multi Parameter Time Stamped Based Coincidence Search) program [33] to construct the RADWARE [34] compatible $\gamma-\gamma$ matrix and γ^3 cube for the analysis of coincidence relationships. Some of the gated spectra obtained from the double and triple γ coincidence data are shown in sections 5.2 and 5.3 while discussing the analysis of various band structures in ^{160}Yb. The relative intensities, I_γ, of the transitions of interest were determined mostly from the appropriately gated projections of the $\gamma-\gamma$ matrix as well as from the total projection in some cases. The $\gamma-\gamma$ angle dependent matrices were prepared for the analysis of DCO, R_θ, and IPDCO ratios using the INGASORT analysis package [35] and the details are discussed below.

The DCO ratios were obtained by using the relation

$$R_{DCO} = \frac{I_{\gamma_1}(\text{at } \theta_1 \text{ when gated by } \gamma_2 \text{ at } \theta_2)}{I_{\gamma_1}(\text{at } \theta_2 \text{ when gated by } \gamma_2 \text{ at } \theta_1)}, \qquad (5)$$

following the prescription of Krämer-Flecken *et al.*, [36]. In the present work, θ_1 and θ_2 were taken as 157° and 90° respectively. The DCO ratios were obtained for the known dipole (779.7 keV) and quadrupole (395.6 keV) transitions which showed the values of 0.44(4) and 1.04(3), respectively, in a gated spectrum of a pure quadrupole transition. Similarly, with a gated spectrum of a pure dipole transition, the ratio was found to be 2.00(8). Most of the transitions of ^{160}Yb were found to have quadrupole nature while some of the inter-band transitions revealed the dipole character. As enough statistical accuracy could not be obtained in the determination of DCO ratios for many of the weak transitions, the R_θ ratio analysis was carried out, where gating with a pure dipole or quadrupole transition is not a prerequisite criterion. This analysis was performed

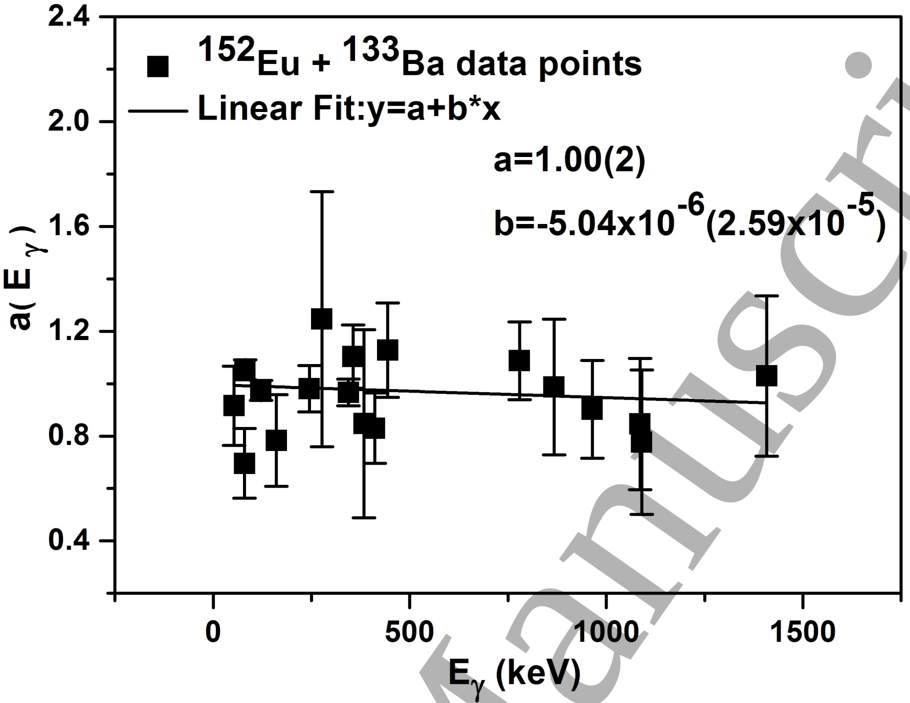

Figure 7. The asymmetry factor, $a(E_\gamma)$, of the array as derived by using the ^{152}Eu and ^{133}Ba sources.

following the procedure detailed in [36, 37], cf. also references therein, and the ratio was calculated as:

$$R_\theta = \frac{I_{\gamma_1}(measured\ at\ \theta_1,\ gated\ over\ all\ angles)}{I_{\gamma_1}(measured\ at\ \theta_2,\ gated\ over\ all\ angles)}. \tag{6}$$

In this analysis, I_{γ_1} (measured at θ_1 (θ_2) = 157° (90°), gated over all angles) corresponds to the γ-ray intensity observed by the detectors at an angle θ_1 (θ_2) by setting gates on the detectors at all other angles. Because of this, all the angular correlation effects are almost completely washed out and the measured γ-ray intensities at both the angles of 157° and 90° follow the ordinary angular distribution features. In the present work, the typical values of this ratio falls within the range of 0.8 - 1.2 for the known dipole-, and 2.18 - 2.57 for the known quadrupole transitions, respectively.

Following the DCO ratio and R_θ ratio analysis, the IPDCO ratio analysis [38, 39, 40, 41] has also been performed in order to determine the electromagnetic nature of the transitions decaying from the excited states of ^{160}Yb. The IPDCO ratio has been calculated as follows:

$$\Delta_{IPDCO} = \frac{a(E_\gamma)N_\perp - N_\parallel}{a(E_\gamma)N_\perp + N_\parallel}, \tag{7}$$

where $N_\perp$ and $N_\parallel$ are the numbers of Compton scattered γ rays in the planes perpendicular-, and parallel to the reaction plane. The a(E_γ) term which is the asymmetry factor arises as a result of the asymmetry in the response of the array and

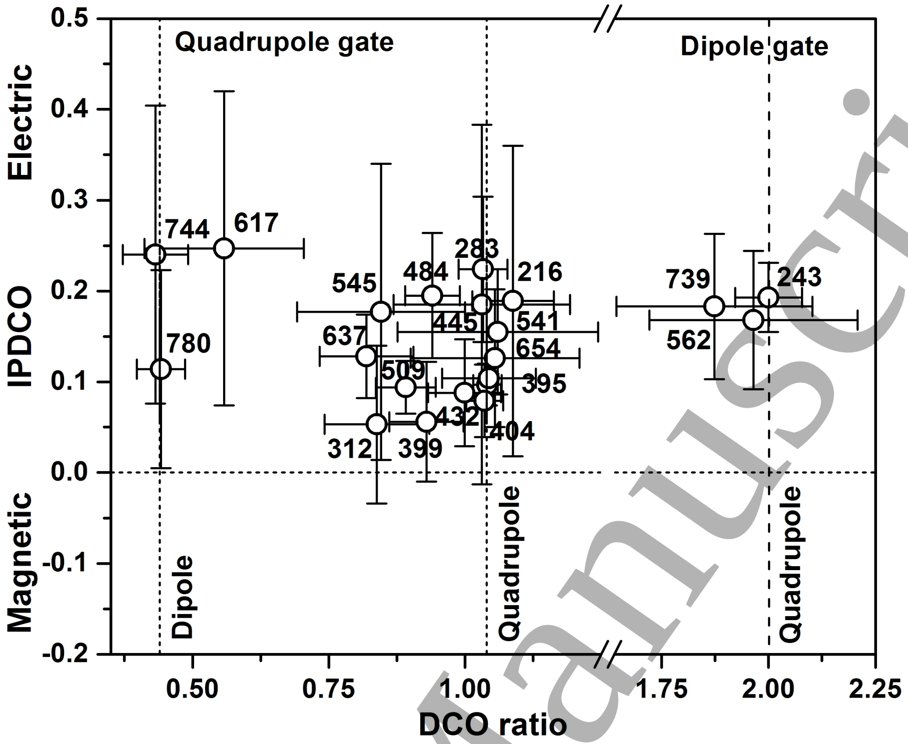

Figure 8. A representative plot for the determination of multipolarities of the γ-transitions from the analysis of DCO and IPDCO ratios. The dotted vertical lines represent the reference values for the dipole and quadrupole transitions in a pure quadrupole gate. The dashed vertical line represent the reference value for a quadrupole transition in a dipole gate. The horizontal line represents the zero value of IPDCO ratio and is shown to guide the eye.

is calculated from the expression $a(E_\gamma) = N_\parallel/N_\perp$, where $N_\perp$ and $N_\parallel$ is taken from the Compton scattered data of ^{152}Eu and ^{133}Ba sources. The correction factor of the array are shown in figure 7. In the present work, the IPDCO ratios were calculated by using the detectors at 90° while setting the gate in all the remaining detectors and on the strong transitions, preferably from below the transition of interest. The multipolarities of particular γ-transitions were evaluated by combining the results from the DCO, R_θ and IPDCO analysis. Figure 8 shows the DCO ratio *vs.* IPDCO ratio for several transitions belonging to the de-excitation scheme of ^{160}Yb.

In the present work, the level scheme of ^{160}Yb has been obtained by using the above information on $\gamma - \gamma$ and $\gamma - \gamma - \gamma$ coincidences, I_γ, DCO, R_θ and IPDCO. The level scheme is shown in figure 9 and 10 whereas the new results are discussed in section 5.3. In addition to the yrast band labelled Band-1, we observed six negative-parity bands labelled Band-2, Band-3, ..., Band-7 – and three positive-parity bands labelled Band-8, Band-9 and Band-10, respectively. The transitions, reported by other authors (see [10, 42, 43]), which were not observed or could not be confirmed from the present work, are shown in bracket and similarly, the levels unobserved by us are indicated with dotted lines. The transitions and energies denoted with dotted lines in red, were reported only

Table 1. Measured branching ratios of some of the observed transitions for which intensities could be measured. The comparisons of the deduced ratios with those from the ENSDF database [42] are also shown (for the details see text).

E_x(keV)	γ_1 & γ_1	$I_{\gamma 1}$	$I_{\gamma 2}$	Ratio	$I_{\gamma 1}$	$I_{\gamma 2}$	Ratio
	(keV)		present work			ENSDF	
2051.2	I(482.7)/I(902.9)	0.7(2)	1.8(4)	0.39(14)	50	100	0.50
2363.0	I(312)/I(435)	2.7(8)	3.0(6)	0.90(32)	62	92	0.67
	I(312)/I(626)	2.7(8)	4.7(12)	0.57(22)	62	100	0.62
2373.6	I(445.6)/I(635.8)	2.9(7)	5.9(15)	0.49(17)	49	100	0.49
2481.5	I(553)/I(744)	2.8(8)	12.6(22)	0.17(7)	23	100	0.23
2579.4	I(205.8)/I(216.4)	1.2(6)	9.2(22)	0.13(7)	14	100	0.14
2764.9	I(389.6)/I(283.4)	2.2(9)	11.8(28)	0.19(9)	28	100	0.28
3747.0	I(608.6)/I(785.1)	14.1(25)	6.8(1)	2.07(37)	100	62	1.61

in the heavy ion experiments [4, 5], whereas those marked in blue were also reported in ^{160}Lu decay experiment [10].

The limiting values of the intensities of transitions reported by other authors but unobserved in the present work are conjectured to be lower than the minimum measurable intensity in the present experiment. The measurable intensities and their limits are discussed in the following section.

5.2. Selective Power of INGA, Reaction used and the limiting intensity branching for unobserved transitions

The Compton suppressed clover detectors of the gamma array used in the present experiment, cf. [33], consisted of four 50 mm × 70 mm HPGe crystals. The array was designed in a way so as to keep the target to crystal distance at 25 cm. Considering all the design parameters of the INGA array, its photo-peak detection efficiency can be ∼5% (at 1.3 MeV) with twenty four Clover detectors placed in the array and for the present work this efficiency was ∼4.2% with twenty Clover detectors used in the experiment. Due to the chosen target-to-detector distance (i.e., increasing the single-hit probability through smaller aperture solid angle) and an adequate number of Clover detectors (i.e., increasing both the total photo-peak efficiency and the granularity of the array), the INGA array is very well suitable for detecting the triple gamma coincidences in the case of experiments for which the gamma multiplicity is of the order of 20.

The reaction cross section of ^{148}Sm(^{16}O,4n)^{160}Yb reaction at E = 90 MeV peaks at an angular momentum of 30 $\hbar$. The following de-excitation of the residual nucleus of ^{160}Yb to its ground state takes place mainly through the emission of stretched E2 γ-transitions. Hence, in the present work, the most probable multiplicity of emitted γ-rays from ^{160}Yb was about 15. This determines the characteristic multiplicity conditions

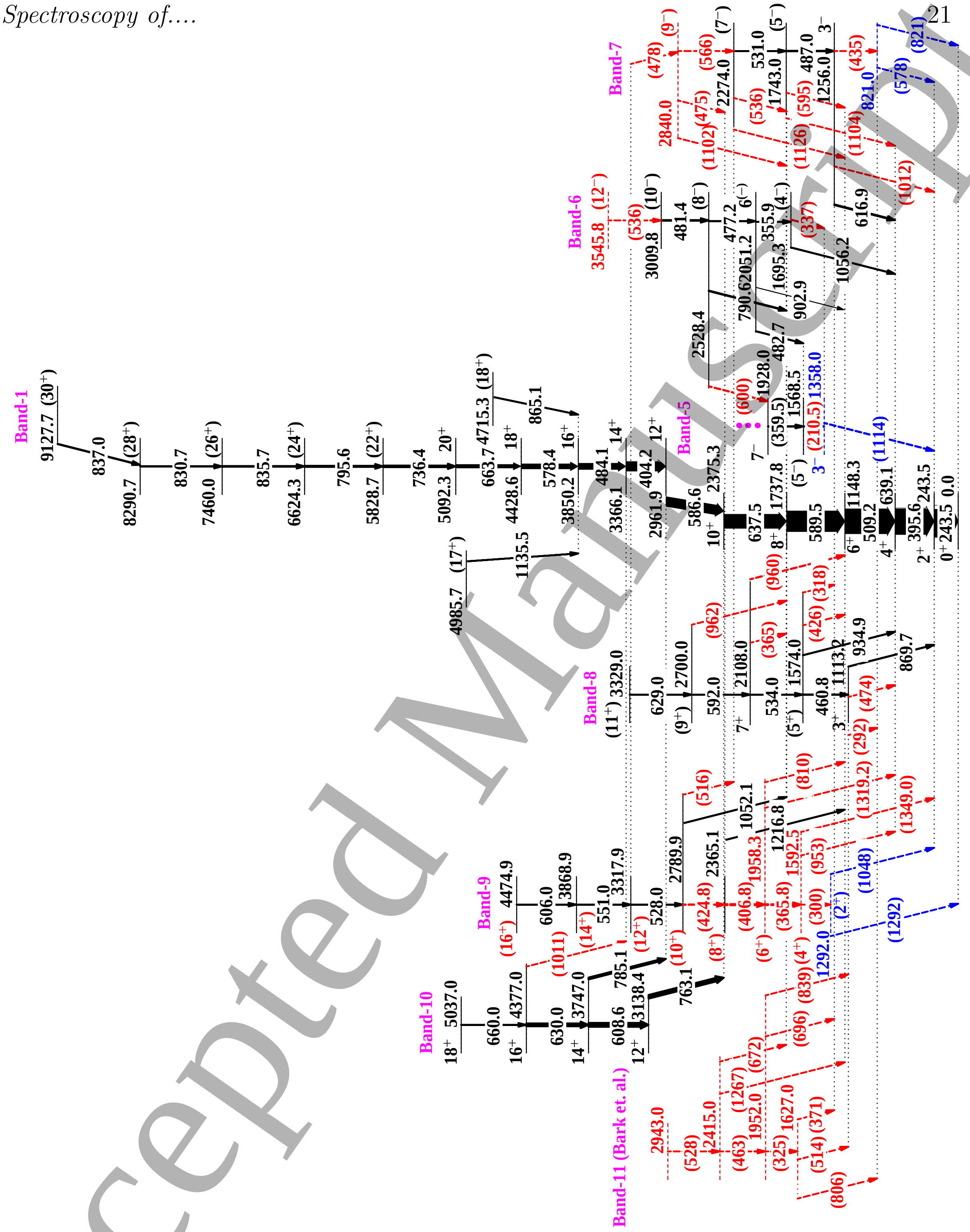

Figure 9. The first part of the level scheme of ^{160}Yb, the Yrast band, the positive parity bands and few of the negative parity bands are shown. The level scheme is divided in two parts for clarity. Band-5 is fully displayed on the second part (figure 10). The transitions which could be placed in the level scheme within our analysis including double gating on triple coincidence data have been shown in black arrows (for the details see text).

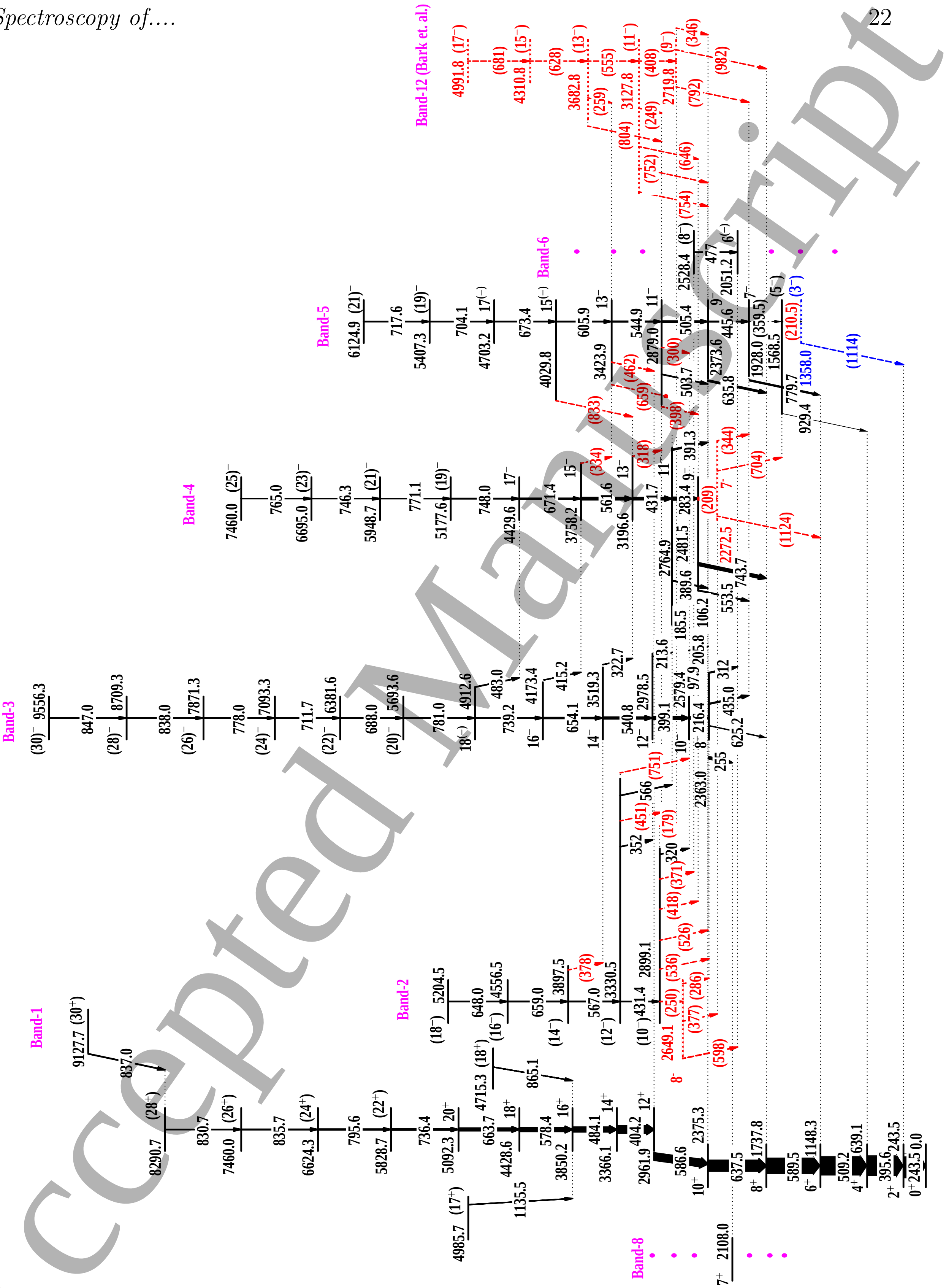

Figure 10. The second part of the ^{160}Yb level scheme, the Yrast band and the negative parity bands (all but Band-6, see figure 9). Band-6 and Band-8 are fully displayed in figure 9. Transitions reported by other authors [4, 5, 10] but unobserved in the present work are shown as red dotted lines and the transition energies written in brackets; the unobserved levels are shown with red dotted lines (see text for details). The color coding is the same as the one used in figure 9.

Table 2. Limiting values of branching ratios for majority of the transitions reported by other authors, cf. [4,5], but not seen in the present work. The limiting values of the branching intensity ratio of transitions for which there exists another transition with known intensity decaying from the same energy level were estimated as well. All the values except the intensities of the unobserved transitions and branching ratio are truncated to first decimal place.

E_x(keV)	γ_1 & γ_2 (keV)	$I_{\gamma1}$ (max.)	$I_{\gamma2}$ Pres. work	Ratio (max.)
1113.2	I(292)/I(869.7)	0.10(5)	0.60(12)	0.17(9)
	I(474)/I(869.7)	0.10(5)	0.60(12)	0.17(9)
1256.0	I(435)/I(616.9)	0.10(5)	2.7(7)	0.04(2)
1568.5	I(210)/I(929.4)	0.10(5)	1.1(3)	0.09(5)
1574.0	I(318)/I(460.8)	0.10(5)	0.8(2)	0.13(7)
	I(426)/I(460.8)	0.10(5)	0.8(2)	0.13(7)
1695.3	I(337)/I(1056.2)	0.10(5)	0.70(18)	0.14(8)
1743.0	I(595)/I(487.0)	0.10(5)	1.9(5)	0.05(3)
	I(1104)/I(487.0)	0.10(5)	1.9(5)	0.05(3)
2108.0	I(365)/I(534.0)	0.10(5)	0.8(2)	0.13(7)
	I(960)/I(534.0)	0.10(5)	0.8(2)	0.13(7)
2274.0	I(536)/I(531.0)	0.10(5)	0.5(1)	0.20(11)
	I(1126)/I(531.0)	0.10(5)	0.5(1)	0.20(11)
2481.5	I(209)/I(743.7)	0.10(5)	12.6(3.0)	0.008(4)
2423.9	I(462)/I(544.9)	0.10(5)	3.4(8)	0.03(2)
2528.4	I(600)/I(477.2)	0.10(5)	1.5(4)	0.07(4)
2789.9	I(516)/I(1052.1)	0.10(5)	0.3(1)	0.33(19)
2879.0	I(398)/I(505.4)	0.10(5)	5.3(13)	0.02(1)
	I(300)/I(505.4)	0.10(5)	5.3(13)	0.02(1)
2899.1	I(179)/I(320)	0.10(5)	0.50(12)	0.20(11)
	I(418)/I(320)	0.10(5)	0.50(12)	0.20(11)
	I(526)/I(320)	0.10(5)	0.50(12)	0.20(11)
	I(371)/I(320)	0.10(5)	0.50(12)	0.20(11)
	I(536)/I(320)	0.10(5)	0.50(12)	0.20(11)
	I(250)/I(320)	0.10(5)	0.50(12)	0.20(11)
3196.6	I(318)/I(431.7)	0.10(5)	10.6(28)	0.01(1)
3330.5	I(451)/I(431.4)	0.10(5)	0.2(1)	0.50(29)
	I(751)/I(431.4)	0.10(5)	0.2(1)	0.50(29)
3423.9	I(659)/I(544.9)	0.10(5)	3.4(8)	0.03(2)
	I(462)/I(544.9)	0.10(5)	3.4(8)	0.03(2)
3758.2	I(334)/I(561.6)	0.10(5)	11.0(2.9)	0.010(5)
3897.5	I(378)/I(567.0)	0.10(5)	2.1(6)	0.05(3)
4029.8	I(833)/I(605.9)	0.10(5)	2.1(5)	0.05(3)
4377.0	I(1011)/I(630.0)	0.10(5)	10.3(24)	0.01(1)

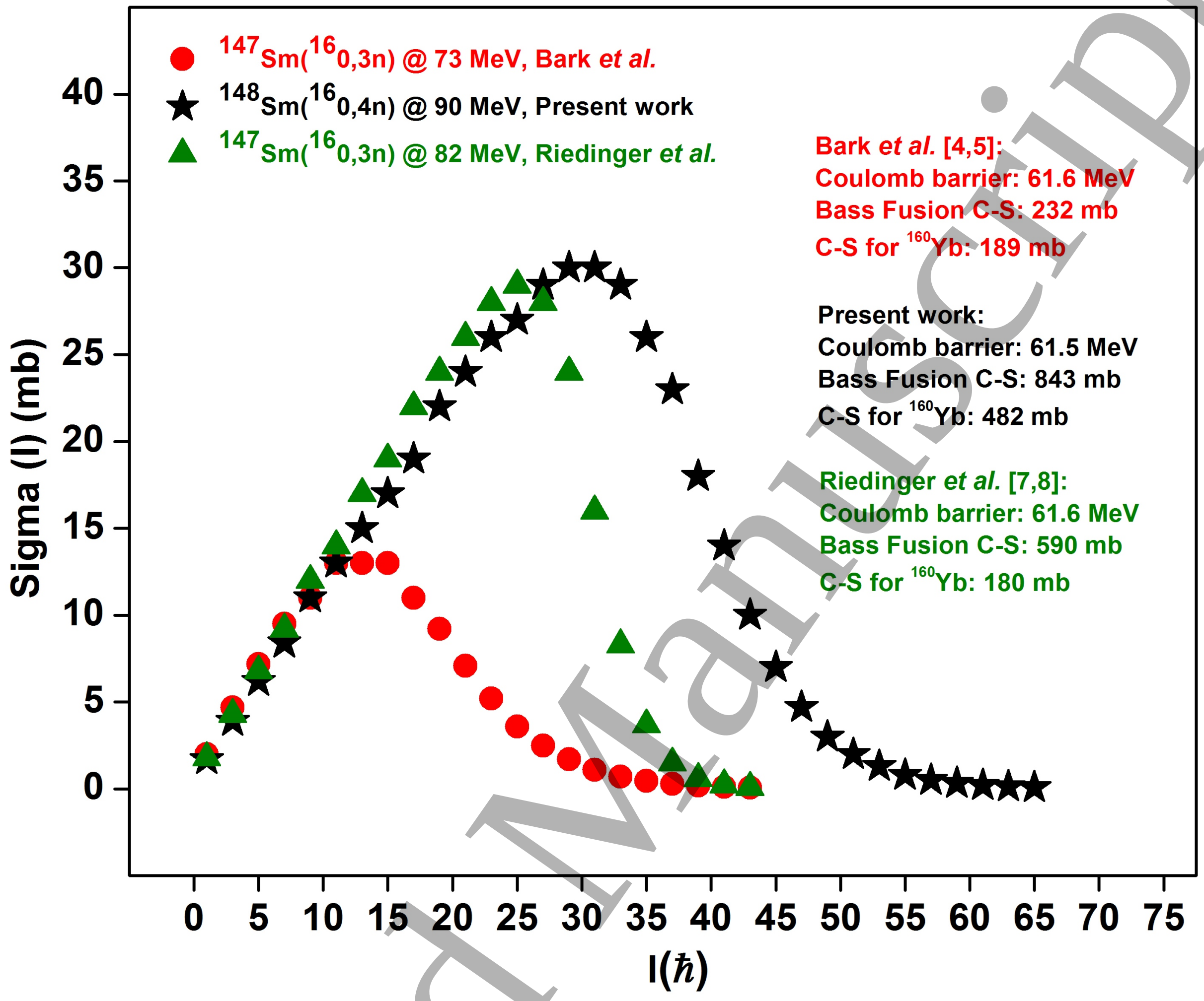

Figure 11. The cross sections estimated with statistical model calculations with PACE IV code, for different heavy ion reactions which are used to populate the excited levels of ^{160}Yb up to date.

under which the triple γ coincidence events were studied. The reaction employed here covers the angular momentum window of the reaction used by Bark and collaborators in [4, 5] with similar cross sections as the one estimated with statistical model of [44] with PACE IV code. This has been displayed in figure 11 where the calculated cross sections of the heavy ion reactions used in different experiments on ^{160}Yb are shown.

This is ensuring a similar feeding pattern of the medium spin states for the two reactions and a possible direct comparison of the obtained decay schemes. However, the HI reactions are not optimised to populate the weak non-yrast levels because in such reactions: (i) nearly all of the band feeding comes from the top and consequently (ii) the low spin states with almost no direct side feeding and very weak feeding from in-band top transitions are difficult to observe. The alpha induced experiments are better suited for the population of such levels in a nucleus, however for ^{160}Yb such a light ion reaction is impossible because of the absence of suitable stable targets. In the present experiment, we were able to collect 6.1×10^9 and 3.5×10^8 prompt double-coincidence and triple-coincidence events respectively. The intensity of 0.1% with respect to the 243.5 keV γ-transition (the most intense ground state feeding transition), has been estimated for the topmost transition of 847.0 keV of Band-3. This is the lowest intensity that could be measured in the present experiment with an acceptable accuracy. The observation of some of the weakest [i.e. about 0.1% compared to 243.5 keV (ground-state transition)] γ-rays known in the level scheme of ^{160}Yb quantify the observation limitations in the present experiment.

In the present work, the Band-1 and Band-3 of ^{160}Yb were observed up to the maximum spin of $30\,\hbar$ and Band-4, up to $25\,\hbar$. The gating conditions of weak transitions associated with the de-excitation of Band-1, Band-3 and Band-4 are presented in figure 13 by adding the cube gates corresponding to all possible combinations of the intra-band transitions of the corresponding bands. The observed transitions which are reported in the ENSDF database [42] but are not observed in [4] have been marked with asterisk in the figure. Moreover, all the weak inter-band transitions from Band-3 to Band-4, reported by Campbell, [45], have been observed in the present work as confirms figure 12 via added double gates from the γ^3 cube. The intensities of these transitions, as estimated in the present work, are smaller than 0.6% of 243.5 keV transition intensity. Although, the presence of the 483.0 keV transition (not observed in [4]) connecting the 18^- level of Band-3 to the 17^- level of Band-4 was confirmed in the present work, its intensity could not be established as this weak transition was the part of a multiplet of the strong 484 keV transition of the yrast band.

Table 1 gives an idea on the extent of population of a particular level in ^{160}Yb and the corresponding detection of the transitions decaying from that particular level, which could be attained in the present experiment, from the measurement of their branching ratios. The said ratios for some of the levels were compared with the available data in ENSDF [42] for which at least two decaying transitions were known in ENSDF with their intensity values. From the table it is clear that the intensity branching ratios for the observed transitions are much in agreement with the branching ratios published in ENSDF. This is expected because branching ratio for a particular level is an observable which is independent of the reactions used for its population.

However, in the present experiment, some of the in-band and inter-band transitions, reported earlier [4, 5] using similar HI reaction, could not be confirmed even with the high selective power of the INGA array. For these unobserved transitions, the limiting value of the possible intensity branching ratios are shown in table 2, by considering the maximum possible intensities for these transitions as the lowest value of intensity (i.e., 0.1% with respect to 243 keV transition) that could be measured in the present work and by considering the error as 50% (maximum error obtained). It is worth mentioning that most of these unobserved transitions tabulated in table 2 are part of multiplets and were reported only in [4, 5].

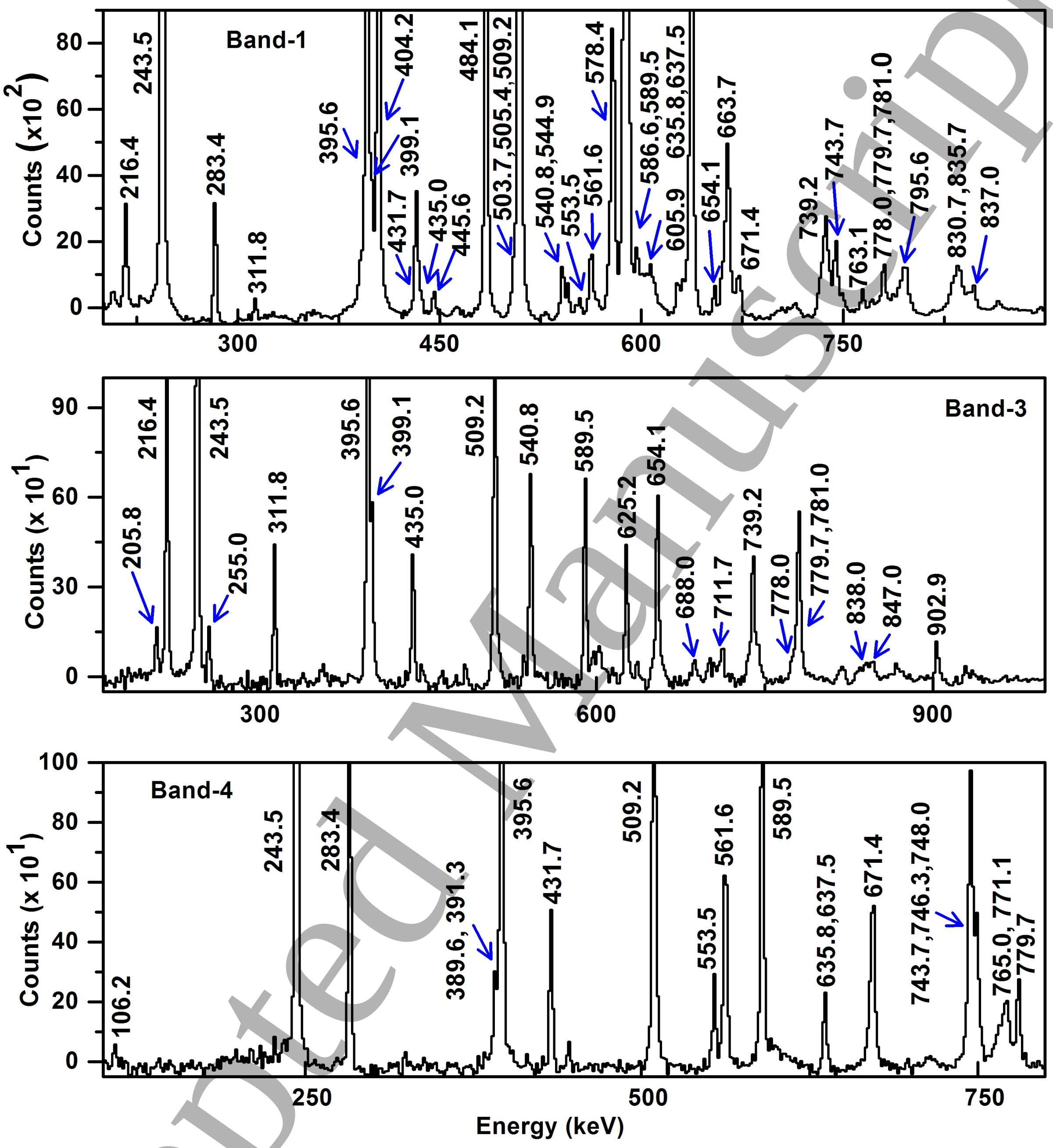

Figure 12. The added cube gates showing the transitions from Band-1 (top panel), Band-3 (middle panel) and Band-4 (bottom panel), populated in the present work. For Band-1, the added gates of [(243&395), (395&509), (509&589), (589&637), (637&587), (587&404), (404&484), (484&578), (578&664), (664&736), (736&796)(in keV)] was used. Similarly, the added gates of (216&399), (399&541), (541&654), (654&739), (739&688), (688&712)(in keV)] was used for Band-3 and the added gates of [(283&432), (432&562), (562&671), (671&748), (748&770)(in keV)] was used for Band-4. The observed transitions arising from the de-excitation of these three bands are marked with their energies. Blue arrows have been used to mark the weakest and close lying γ-rays.

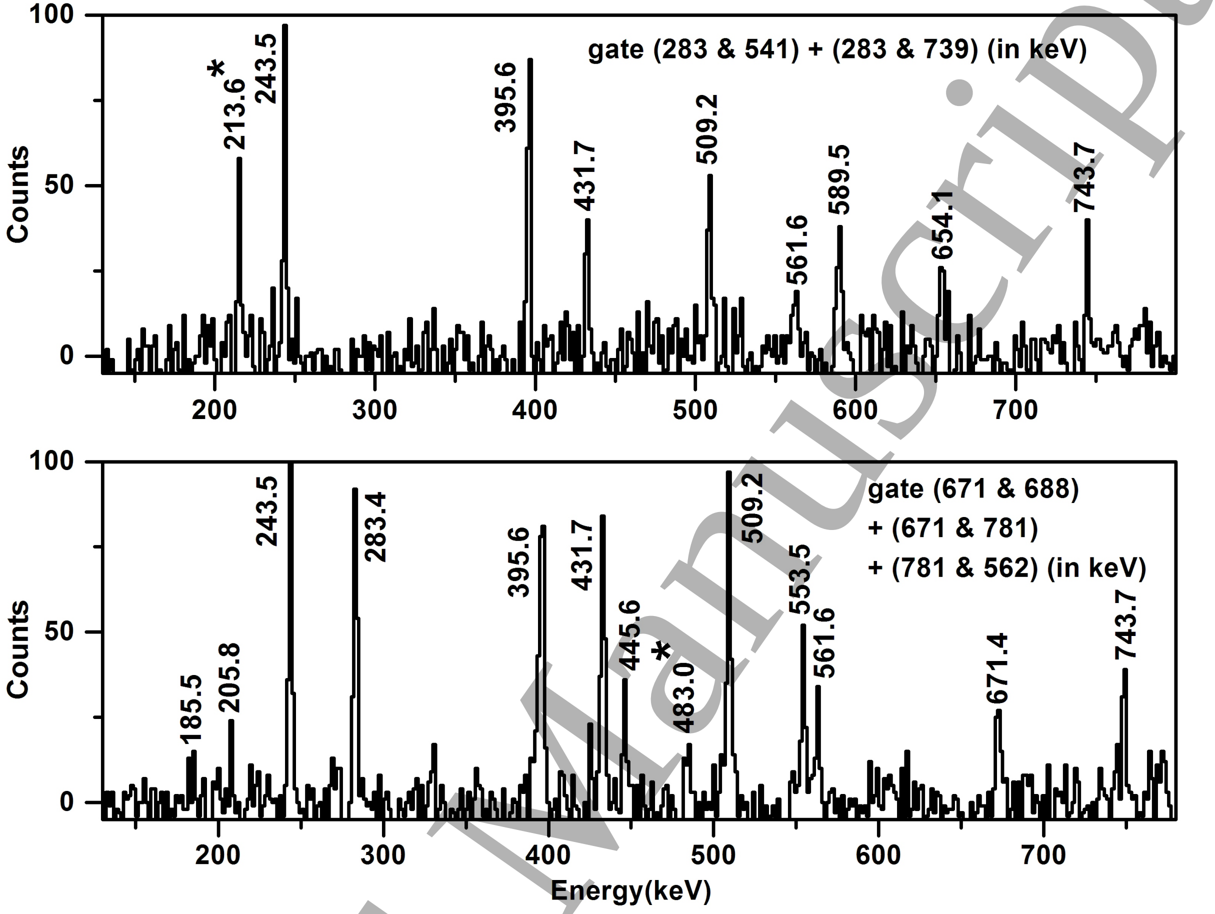

Figure 13. The added cube gates showing the inter-band transitions decaying from Band-3 to Band-4. The ones at 213.6 keV and 483.0 keV, marked with asterisks, represent the decay from 12^- and 18^- levels of Band-3.

5.3. Level Scheme of ^{160}*Yb and the Band structures*

The energies, relative intensities, DCO ratios, R_θ and IPDCO ratios for the transitions observed in the present experiment have been tabulated in table 3 along with other relevant details.

Table 3: The spectroscopic results for the γ-transitions observed in the present experiment on ^{160}Yb.

E_i (keV)	J_i^π	$\rightarrow$	J_f^π	E_γ† (keV)	I_γ‡	DCO§ (err)(gate)	IPDCO (err)	R(θ) (err)	Mult.
2579.4	10^-	$\rightarrow$	9^-	97.9	0.4				(M1)
2481.5	9^-	$\rightarrow$	10^+	106.2	0.2				(E1)
2764.9	11^-	$\rightarrow$	10^-	185.5	0.2				(M1)
2579.4	10^-	$\rightarrow$	9^-	205.8	1.2				(M1)
2978.5	12^-	$\rightarrow$	11^-	213.6	0.6				(M1)
2579.4	10^-	$\rightarrow$	8^-	216.4	9.2	1.09(8)(Q)	+0.19(17)	2.31(8)	E2
243.5	2^+	$\rightarrow$	0^+	243.5	100	2.00(8)(D)	+0.19(4)	2.51(6)	E2
2363.0	8^-	$\rightarrow$	7^+	255.0	0.8	0.53(8)(Q)		1.23(18)	E1
2764.9	11^-	$\rightarrow$	9^-	283.4	11.8	1.03(5)(Q)	+0.22(8)	2.42(9)	E2
2363.0	8^-	$\rightarrow$	$6^{(-)}$	311.8	2.7	0.84(10)(Q)	+0.05(9)	2.65(12)	E2
2899.1	(10^-)	$\rightarrow$	10^-	319.7	0.5				(M1)
3519.3	14^-	$\rightarrow$	13^-	322.7	0.5				(M1)
3330.5	(12^-)	$\rightarrow$	12^-	352.0	0.3				(M1)
2051.2	$6^{(-)}$	$\rightarrow$	(4^-)	355.9	0.6				(E2)
1928.0	7^-	$\rightarrow$	(5^-)	359.5	0.4				(E2)
2764.9	11^-	$\rightarrow$	10^+	389.6	2.2				(E1)
2764.9	11^-	$\rightarrow$	9^-	391.3	4.4				(E2)
639.1	4^+	$\rightarrow$	2^+	395.6	91.7	1.04(3)(Q)	+0.10(3)	2.45(6)	E2
2978.5	12^-	$\rightarrow$	10^-	399.1	12.7	0.93(7)(Q)	+0.06(7)	2.46(11)	E2
3366.1	14^+	$\rightarrow$	12^+	404.2	33.3	1.04(3)(Q)	+0.08(4)	2.51(12)	E2
4173.4	16^-	$\rightarrow$	15^-	415.2	0.1				(M1)
2789.9				(424.8)					
3330.5	(12^-)	$\rightarrow$	(10^-)	431.4	0.2				(E2)
3196.6	13^-	$\rightarrow$	11^-	431.7	10.6	1.00(7)(Q)	+0.09(6)	2.24(13)	E2
2363.0	8^-	$\rightarrow$	7^-	435.0	3.0	0.49(7)(Q)	+0.11(9)	1.20(5)	E2+M1
2373.6	9^-	$\rightarrow$	7^-	445.6	2.9	1.03(16)(Q)	+0.19(20)	2.74(21)	E2
1574.0	(5^+)	$\rightarrow$	3^+	460.8	0.8				(E2)
2528.4	(8^-)	$\rightarrow$	$6^{(-)}$	477.2	1.5				(E2)
3009.8	(10^-)	$\rightarrow$	(8^-)	481.4	2.5				(M1)
2051.2	$6^{(-)}$	$\rightarrow$	(5^-)	482.7	0.7				(M1)
4912.6	$18^{(-)}$	$\rightarrow$	17^-	483.0*	<0.1				M1
3850.2	16^+	$\rightarrow$	14^+	484.1	21.9	0.94(5)(Q)	+0.20(7)	2.14(5)	E2
1743.0	(5^-)	$\rightarrow$	3^-	487.0	1.9				(E2)
2879.0	11^-	$\rightarrow$	10^+	503.7	1.4				(E1)
2879.0	11^-	$\rightarrow$	9^-	505.4	5.3	1.33(38)(D)			E2
1148.3	6^+	$\rightarrow$	4^+	509.2	87.6	0.89(6)(Q)	+0.09(3)		E2
3317.9				528.0	0.5				
2274.0	(7^-)	$\rightarrow$	(5^-)	531.0	0.5				(E2)
2108.0	7^+	$\rightarrow$	(5^+)	534.0	0.8				(E2)
3519.3	14^-	$\rightarrow$	12^-	540.8	8.2	1.06(19)(Q)	+0.16(7)	2.32(11)	E2
3423.9	13^-	$\rightarrow$	11^-	544.9	3.4	0.85(16)(Q)	+0.18(17)	1.97(11)	E2
3868.9				551.0	0.5				

TABLE III: continued...

E_i (keV)	J_i^π	→	J_f^π	E_γ† (keV)	I_γ‡	DCO§ (err)(gate)	IPDCO (err)	R(θ) (err)	Mult.
2481.5	9^-	→	7^-	553.5	2.2	0.94(17)(Q)		2.11(15)	E2
3758.2	15^-	→	13^-	561.6	11.0	1.97(25)(D)	+0.17(8)	2.11(14)	E2
3330.5	(12^-)	→	11^-	565.6	1.3				(M1)
3897.5	(14^-)	→	(12^-)	567.0	2.1				(E2)
4428.6	18^+	→	16^+	578.4	18.0			2.45(12)	E2
2961.9	12^+	→	10^+	586.6	33.9	0.87(4)(Q)	+0.12(1)	2.23(5)	E2
1737.8	8^+	→	6^+	589.5	73.0	1.04(9)(Q)	+0.10(1)	2.34(4)	E2
2700.0	(9^+)	→	7^+	592.0	0.1				(E2)
4029.8	$(15)^-$	→	13^-	605.9	2.1			2.26(18)	(E2)
4474.9				606.0	0.4				
3747.0	14^+	→	12^+	608.6	14.1				E2
1256.0	3^-	→	4^+	616.9	2.7	0.56(15)(Q)	+0.25(18)	1.21(13)	E1
2363.0	8^-	→	8^+	625.2	4.7	1.34(27)(Q)	-0.07(10)	2.86(16)	(M2)
3329.0	(11^+)	→	(9^+)	629.0	0.1				(E2)
4377.0	16^+	→	14^+	630.0	10.3			2.54(58)	E2
2373.6	9^-	→	8^+	635.8	5.9	0.59(11)(Q)			E1
2375.3	10^+	→	8^+	637.5	49.8	0.82(9)(Q)	+0.13(5)		E2
5204.5	(18^-)	→	(16^-)	648.0	1.2				(E2)
4173.4	16^-	→	14^-	654.1	4.9	1.06(16)(Q)	+0.13(8)	2.18(24)	E2
4556.5	(16^-)	→	(14^-)	659.0	2.1				(E2)
5037.0	18^+	→	16^+	660.0	1.5				(E2)
5092.3	20^+	→	18^+	663.7	12.7	0.72(5)(Q)	+0.18(7)	2.21(14)	E2
4429.6	17^-	→	15^-	671.4	3.4	0.73(11)(Q)	+0.11(7)	2.64(22)	(E2)
4703.2	$(17)^-$	→	$(15)^-$	673.4	1.5			2.03(17)	(E2)
6381.6	$(22)^-$	→	$(20)^-$	688.0	1.0				(E2)
5407.3	$(19)^-$	→	$17^{(-)}$	704.1	0.7				(E2)
7093.3	$(24)^-$	→	$(22)^-$	711.7	0.4				E2
6124.9	$(21)^-$	→	$(19)^-$	717.6	0.4				(E2)
5828.7	(22^+)	→	20^+	736.4	5.8	1.39(18)(Q)	+0.15(11)	2.52(15)	(E2)
4912.6	$18^{(-)}$	→	16^-	739.2	2.9	1.87(23)(D)	+0.18(8)	2.31(36)	E2
2481.5	9^-	→	8^+	743.7	12.6	0.43(6)(Q)	+0.24(17)	1.46(10)	E1
6695.0	$(23)^-$	→	$(21)^-$	746.3	0.5				(E2)
5177.6	$19^{(-)}$	→	17^-	748.0	2.0	0.51(17)(Q)		2.01(23)	(E2)
3138.4	12^+	→	10^+	763.1	12.9			1.97(22)	E2
7460.0	$(25)^-$	→	$(23)^-$	765.0	0.4				(E2)
5948.7	$(21)^-$	→	$19^{(-)}$	771.1	0.6			2.49(25)	(E2)
7871.3	$(26)^-$	→	$(24)^-$	778.0	0.3				(E2)
1928.0	7^-	→	6^+	779.7	8.9	0.44(5)(Q)	+0.11(11)	1.11(5)	E1
5693.6	$(20)^-$	→	$18^{(-)}$	781.0	1.0				(E2)
3747.0	14^+	→	12^+	785.1	6.8				E2
2528.4	(8^-)	→	8^+	790.6	2.2				(E1)
6624.3	(24^+)	→	(22^+)	795.6	4.1	0.74(10)(Q)	+0.05(8)	2.57(8)	E2
8290.7	(28^+)	→	(26^+)	830.7	1.6				(E2)
7460.0	(26^+)	→	(24^+)	835.7	2.6				(E2)
9127.7	(30^+)	→	(28^+)	837.0	1.6				(E2)

TABLE III: continued...

E_i (keV)	J_i^π	$\rightarrow$	J_f^π	E_γ† (keV)	I_γ‡	DCO§ (err)(gate)	IPDCO (err)	R(θ) (err)	Mult.
8709.3	$(28)^-$	$\rightarrow$	$(26)^-$	838.0	0.2				(E2)
9556.3	$(30)^-$	$\rightarrow$	$(28)^-$	847.0	0.1				(E2)
4715.3	(18^+)	$\rightarrow$	16^+	865.1	0.5				M1
1113.2	3^+	$\rightarrow$	2^+	869.7	0.6				E1
2051.2	$6^{(-)}$	$\rightarrow$	6^+	902.9	1.8	0.76(14)(Q)		2.35(35)	E1
1568.5	(5^-)	$\rightarrow$	4^+	929.4	1.1			0.98(27)	E1
1574.0	(5^+)	$\rightarrow$	4^+	934.9	0.9				(E1)
2789.9	(8^+)	$\rightarrow$	8^+	1052.1	0.3				(E2)
1695.3	(4^-)	$\rightarrow$	4^+	1056.2	0.7				(E1)
4985.7	(17^+)	$\rightarrow$	16^+	1135.5	0.4				(M1)
2365.1	(6^+)	$\rightarrow$	6^+	1216.8	0.2				(E2)

†‡§

The development of the respective band structures are shown by adding the double gates in all possible combinations among the in-band transitions, wherever possible. These added gates are shown in the following figures, viz., figure 14 to figure 20, where all the unobserved transitions have been marked in red.

5.3.1. Negative Parity Bands: Band-2, Band-4, Band-5, Band-6 and Band-7 The population of the states of Band-2 is shown in figure 14 and all the in-band transitions of this band could be confirmed except some of the inter connecting transitions to the other negative parity bands.

The odd-spin Band-5 and the even-spin Band-6 are connected mainly to the yrast band (Band-1) by several $\Delta I = 1$ and $\Delta I = 0$ E1-transitions, respectively which is shown in figure 9 and 10. The structure of Band-5 as observed in the present work, has been discussed separately in [46] along with another band that was reported earlier [4] but not observed in the present experiment. The structure of Band-6 has been illustrated in figure 15. The 1358 keV 3^- level of Band-5, reported in [4], was observed in the decay of ^{160}Lu [10] but in no other heavy ion data [42]. In the present work, the existence of this level could not be confirmed either, possibly because of lack of direct feeding from the reaction at low spin. The 1568.5 keV (5^-) level, decaying through 929.4 keV transition, has been confirmed from the cube data. This level is fed by the 482.7 keV transition decaying from the $6^{(-)}$ level of Band-6 and 359.5 keV transition from the 7^- level of Band-5. However, the added gate from γ^3 cube with all possible combinations of the intra-band transitions of Band-5, shows very weak signatures of the presence of the 359.5

---

† The uncertainties in the deduced energy values are, typically, of ±(0.1-0.2) keV.

‡ The uncertainty in the intensity values, originated due to peak fitting, come out to be on average less to ∼3%. For some cases, weak transitions and/or multiplets, these uncertainties could range up to ∼30% or even up to ∼50% for the weakest ones.

§ The nature of the gated transition has been indicated using letters, Q for quadrupole and D for dipole.

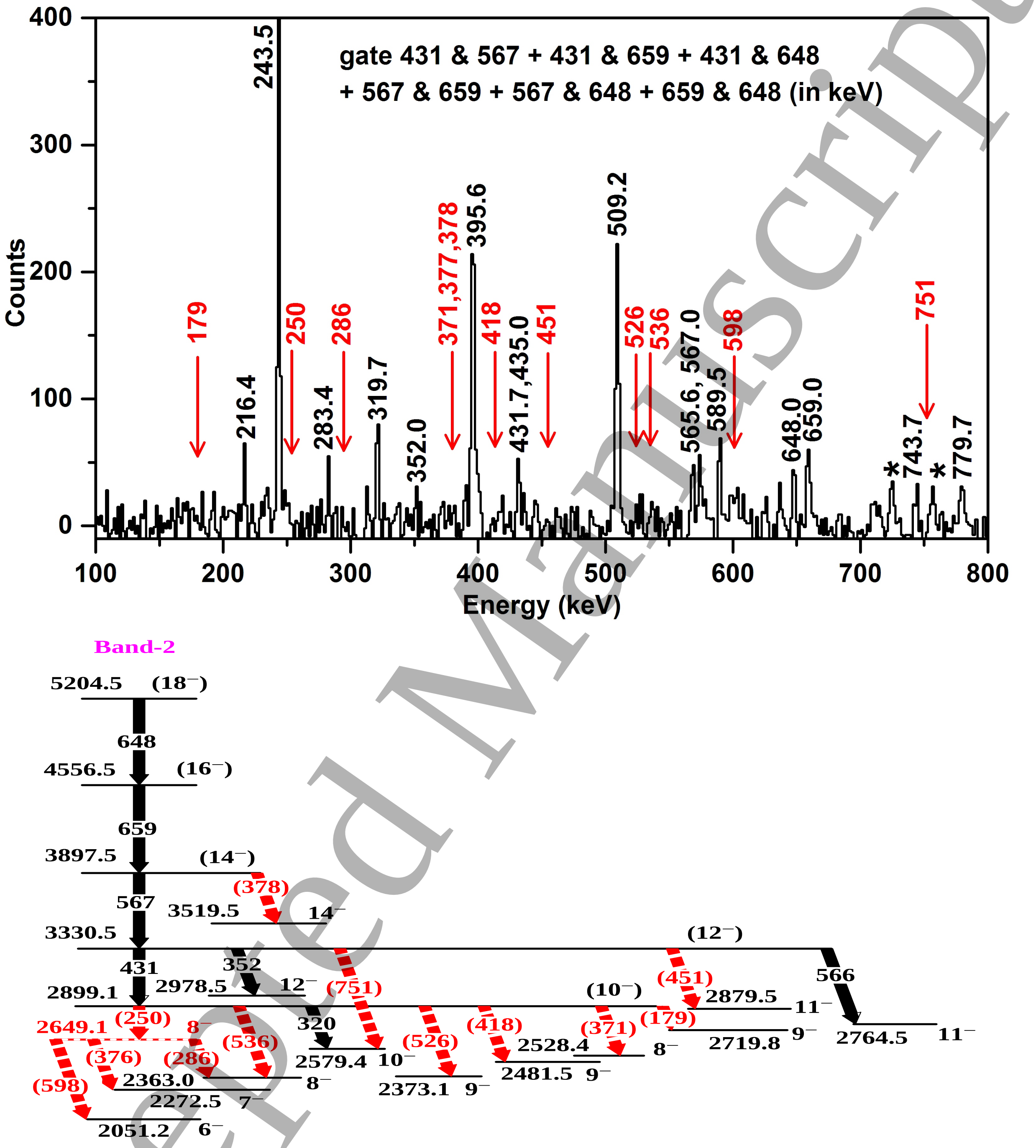

Figure 14. The spectrum corresponding to the added cube gates of all six possible combinations of the intra-band transitions of Band-2, which are de-exciting the levels above (10$^-$), is shown. The decay of Band-2 is also shown in the partial level scheme displayed at the bottom of the gated spectrum. The transitions shown with black arrows in the level scheme are clearly visible in the gated spectrum and are marked with black text. The transitions marked with red arrows in the levels scheme are the ones that were proposed by other authors but could not be confirmed in the present work. The position of these transitions in the gated spectrum are shown with red arrows and red text. The γ rays shown in the gated spectrum and marked with * could not be placed in the level scheme of ^{160}Yb. The thickness of the transitions given in the decay scheme are not in proportion to their actual intensities. See figure 9 for details on full level scheme.

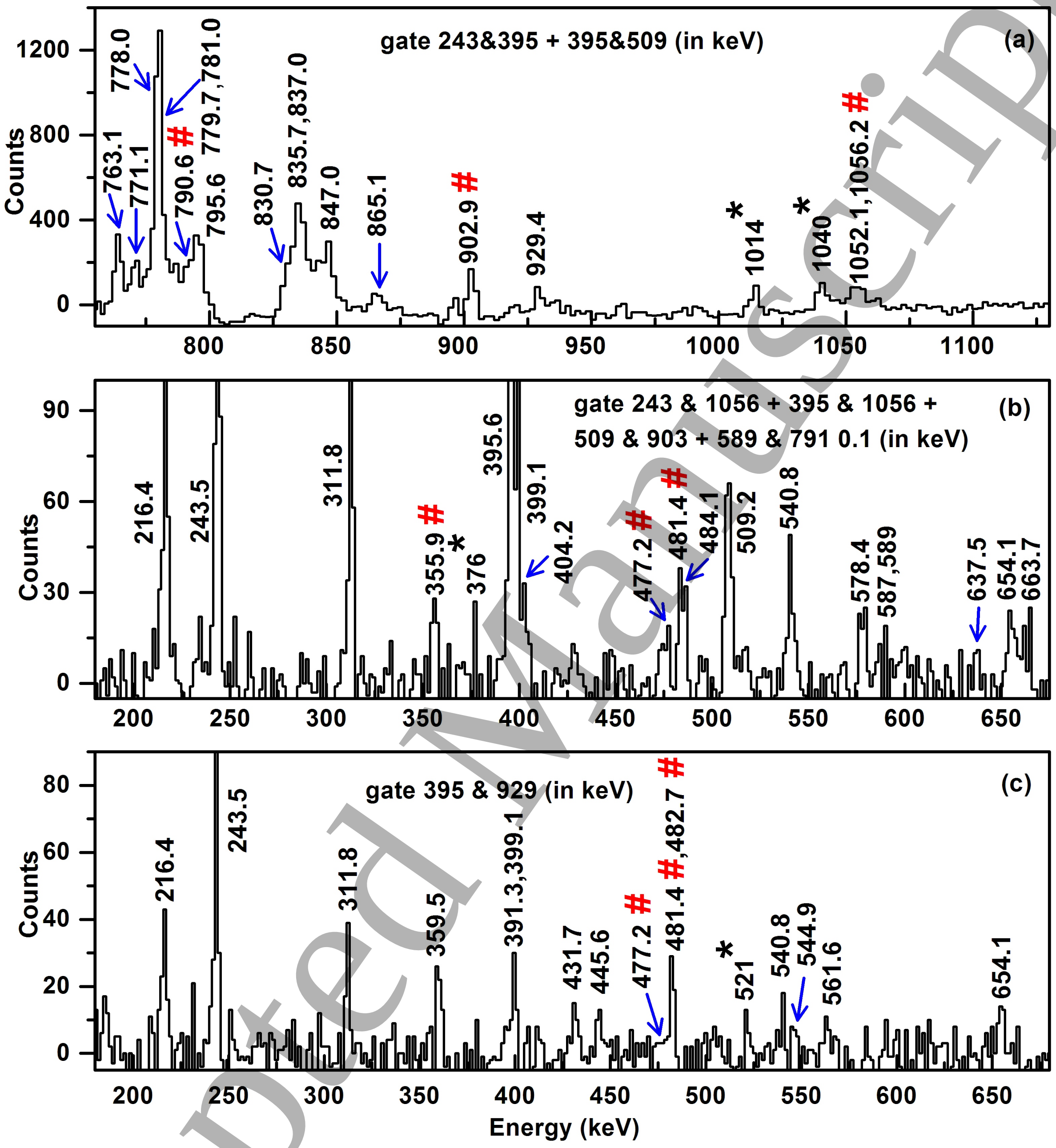

Figure 15. The added cube gates show the γ-rays related to the de-excitation of Band-6 as observed in the present work. The top panel (a) shows the presence of three inter-band transitions (790.6, 902.9 and 1056.2 keV) decaying from Band-6 to the yrast band; the middle and bottom panels, (b) and (c) respectively, show all the intra-band transitions (355.9, 477.2 and 481.4 keV) of Band-6 and one inter-band transition (482.7 keV) decaying from Band-6 to Band-5. All the intra-band and inter-band transitions of Band-6 are marked with the symbol "#". The transitions marked with asterisks could not be placed in the levels scheme of ^{160}Yb. Blue arrows have been used to mark the weakest and close lying γ-rays.

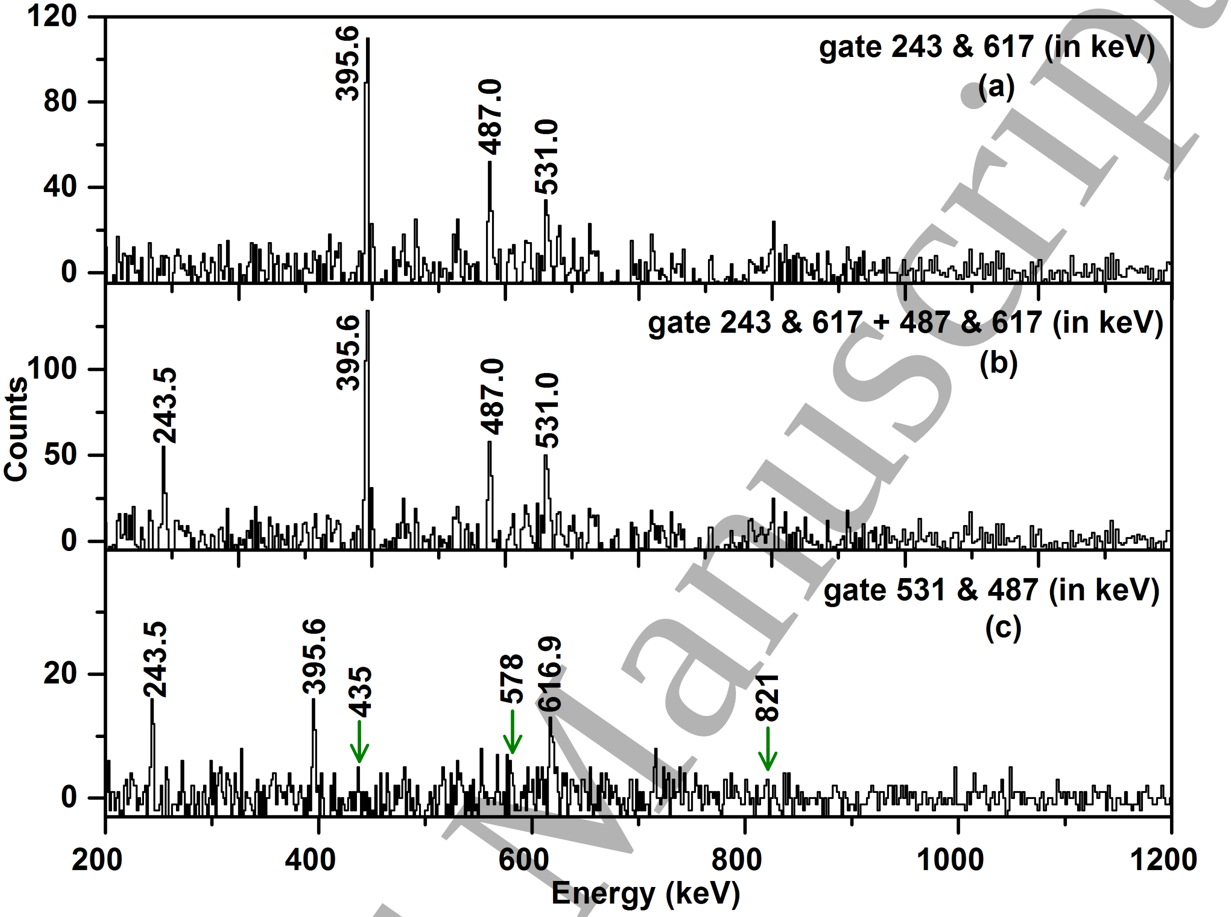

Figure 16. The transitions observed from three different cube gates, shown in three panels ((a), (b) and (c)), indicate the population of the 1256, 1743 and 2274 keV levels of Band-7 as observed in the present experiment. The bottom panel (c) indicates that the population of the 821 keV, 1^- state and its connection to Band-7 could not be confirmed in the present work because of no indication of the 435, 578 and 821 keV transitions. The position of these γ-rays are indicated by green arrows.

and 929.4 keV γ rays. We believe that this is due to the fact that almost full intensity of the 1928.0 keV 7^- level of Band-5 decays through the 779.7 keV E1-transition and compared to that, the intensity decaying through the intra-band E2-transition of 359.5 keV is almost negligible. This is also apparent from the relative intensity values of these two transitions, as given in table 3. The 359.5 keV transition has also been shown as dotted in the level scheme, given in figure 9 and 10.

It was observed that there is no connection between Band-4 and Band-5 beyond spin $11\hbar$, as evident from figure 17. The 833 keV transition has been found to be a contaminant transition in coincidence with all the transitions belonging to Band-4 and Band-5. Similarly, the 659 keV transition is observed in coincidence with 283.4 keV of Band-4 and all the transitions of Band-2 from the analysis of the $\gamma - \gamma$ matrix and γ^3 cube. The present work confirms that there is a single 659.0 keV transition in the level

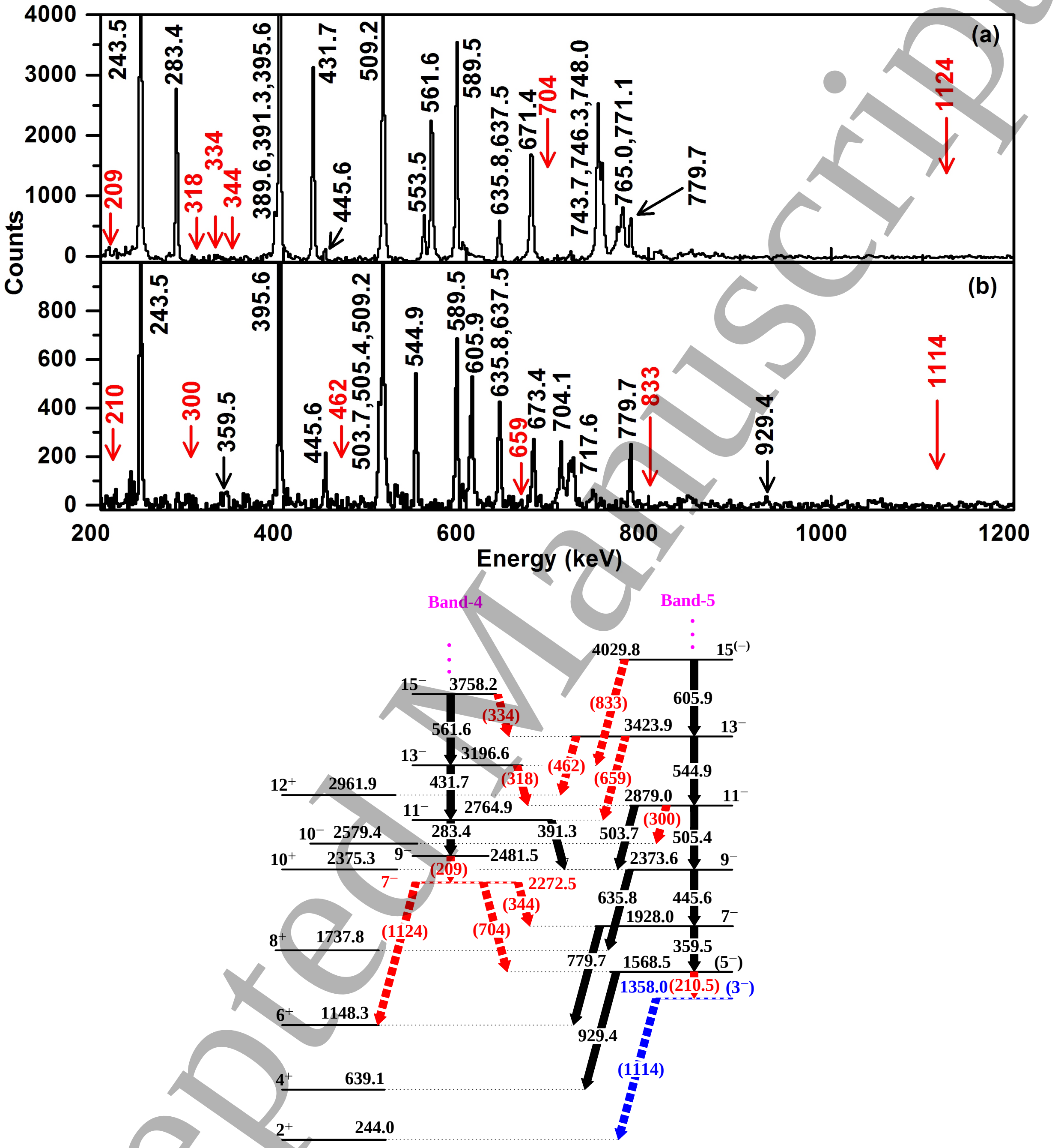

Figure 17. (a) The spectrum corresponding to the added cube gates of all possible combinations (28 in total) of the in-band transitions of Band-4 is shown. (b) The spectrum corresponding to added cube gates made by all possible combination (28 in total) of the in-band transitions of Band-5 is shown. The partial decay schemes of Band-4 and Band-5 are also shown at the bottom. The magnified level scheme here only displays the low spin part of the bands which extend above spin 15^{-} as indicated by the vertical ellipsis (see figure 9). The transitions shown with black arrows in the level scheme are clearly visible in the gated spectra and are marked with black text. The transitions marked with red and blue arrows in the level scheme are the ones that were proposed by other authors, viz. [4, 5] and [10], respectively, but could not be confirmed in the present work. The position of these transitions in the gated spectrum are shown with red arrows and red text. The thickness of the transitions given in the decay scheme are not in proportion to their actual intensities. See figure 9 for details on full level scheme.

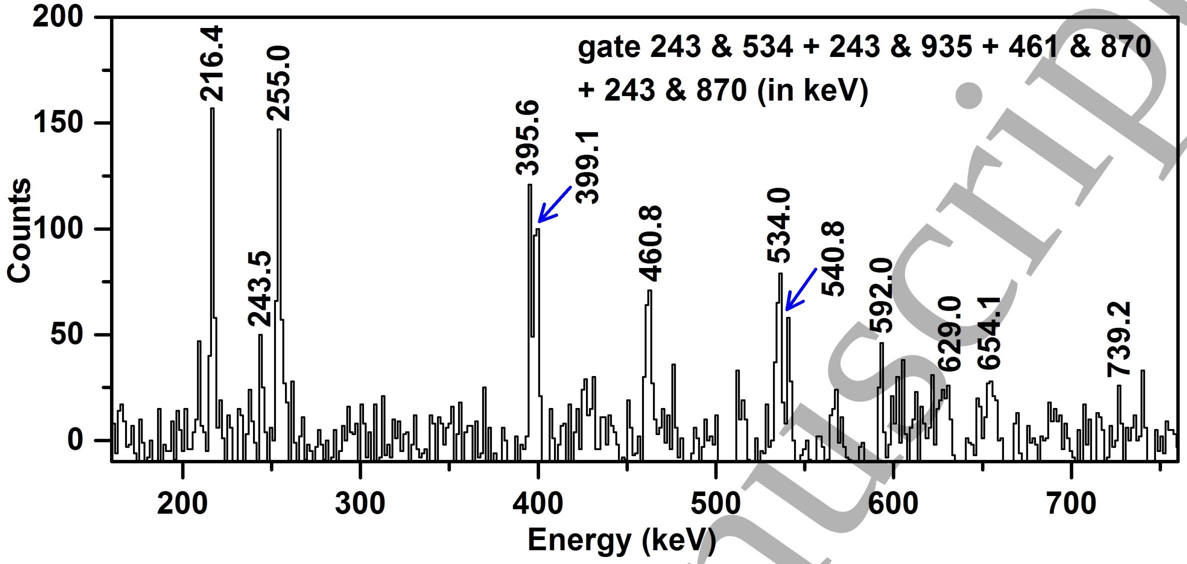

Figure 18. The added cube gates of [(243&534) + (243&935) + (461&870) + (243&870) (in keV)] is shown. The γ transitions observed in these added gates confirm the population of the odd-spin positive-parity Band-8 on top of the 1113.2 keV, 3^+ level and are marked with their energy values. Blue arrows have been used to mark close lying peaks. The 255 keV transition is observed in these added gates as this transition connects the positive parity Band-8 to the negative parity Band-3.

scheme of ^{160}Yb and it belongs to Band-2; even from the cube gate, no sign for the presence of the 659 keV transition, connecting the 13^- level of Band-5 and 11^- level of Band-4, could be obtained.

The odd-spin negative-parity Band 7 is built on the 1256 keV and development of the band has been shown in figure 16. The spin-parity $I^\pi = 3^-$ identification of the 1256 keV level was adopted in [42] after the experimental work on the decay of ^{160}Lu [10]. In the present work also we have measured for the first time the E1 character of the 616.9 keV line by gamma-ray spectroscopic techniques confirming the $I^\pi = 3^-$ assignment of ENSDF. The Band-7 was, however, proposed as the positive parity gamma band [5] with 821 keV, 2_2^+ level as the band head, by making the 1256 keV level as 4^+ and connecting the 1256 keV level to the 821 keV level by a 435 keV transition. In our cube data, we could not observe this connection of the 1256 keV level to the 821 keV, 2_2^+ level, as the presence of 435 keV transition could not be confirmed.

5.3.2. Positive Parity Bands: Band-8, Band-9 and Band-10 The positive-parity side bands were observed up to spins 11 $\hbar$ for Band-8, and 18 $\hbar$ for Band-10, respectively and no spin-parity assignment has been possible for Band-9. The population of Band-8, Band-9 and Band-10 are shown in figure 18, figure 19 and figure 20 respectively.

The odd-spin positive-parity sequence of Band-8 has been developed on 1113.2 keV level as observed from the above gated spectra. The assigned spin-parity combination for

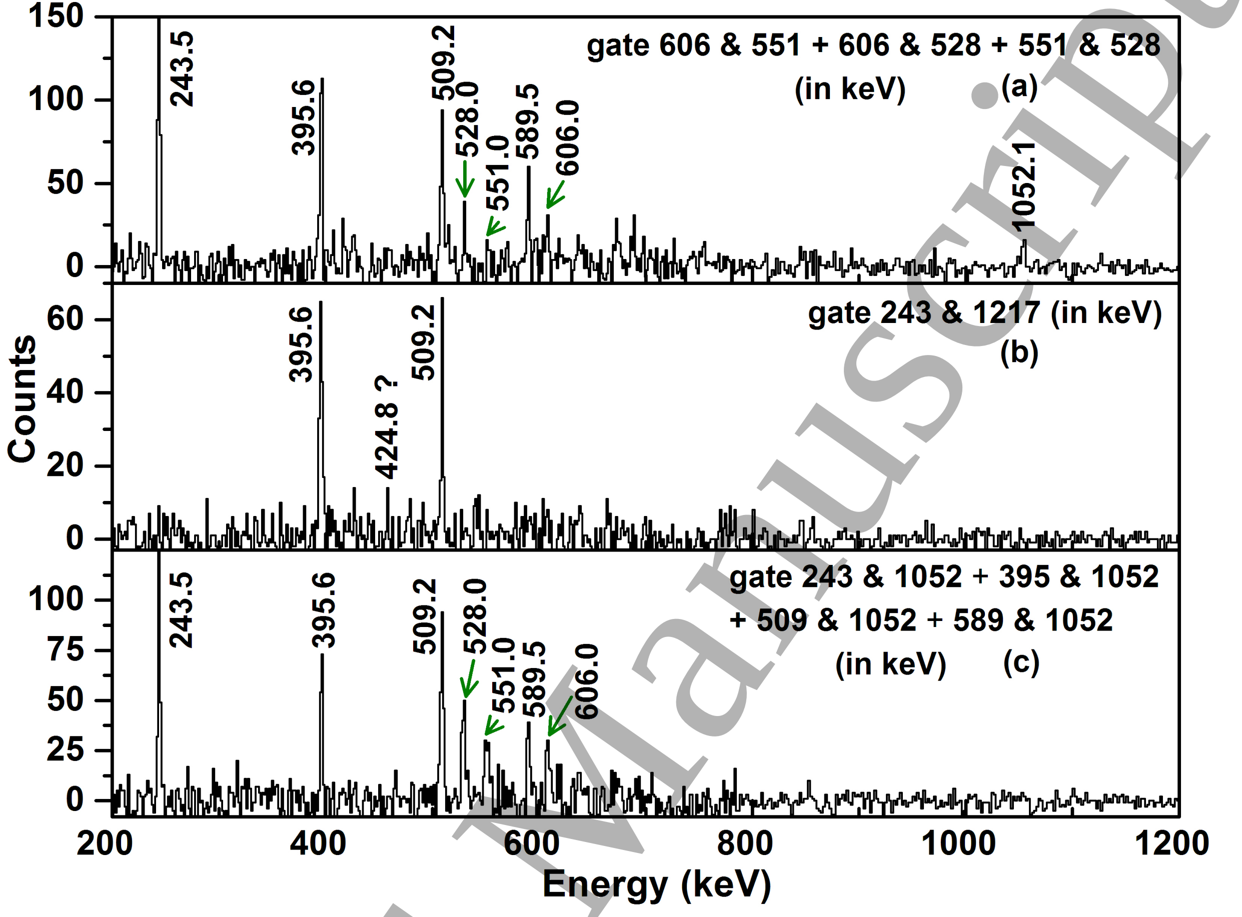

Figure 19. The γ-rays observed in the cube gates displayed in (a), (b) and (c) indicate the population of states with energy values ranging from 2365.1 to 4474.9 keV of Band-9. Due to the very weak indication of the 424.5 keV transition between 2789.9 keV and 2365.1 keV levels, as observed from the gate in panel (b), it is shown in bracket in the level scheme (see figure 9). Green arrows have been used to mark the in-band transitions. The spins of the Band-9 states could not be determined in this work.

Band-8 comes from the confirmed spin-parity of 1113.2 keV level as 3^+ from the earlier works [10, 42] where this level is identified at 1112.0 keV, and from the E1-character of the 255.0 keV transition, assigned in the present work.

The Band-9 was populated up to 4474.9 keV excitation, however, its spins and parities could not be determined in the present experiment. This band was reported also in [5], where it was assigned even-spins and positive parity, and interpreted as β-vibration band. However, in the present work, the levels placed in this band below 2365.1 keV in [5] could not be established and these levels are shown with dotted lines. Consequently, no connection of the band is found with the 1086.1 keV, (0_2^+) or 1292.8 keV, 2_3^+ level of ^{160}Yb [42]. A new level at 4474.9 keV has, however, been observed in this band, which was not known prior to the present work.

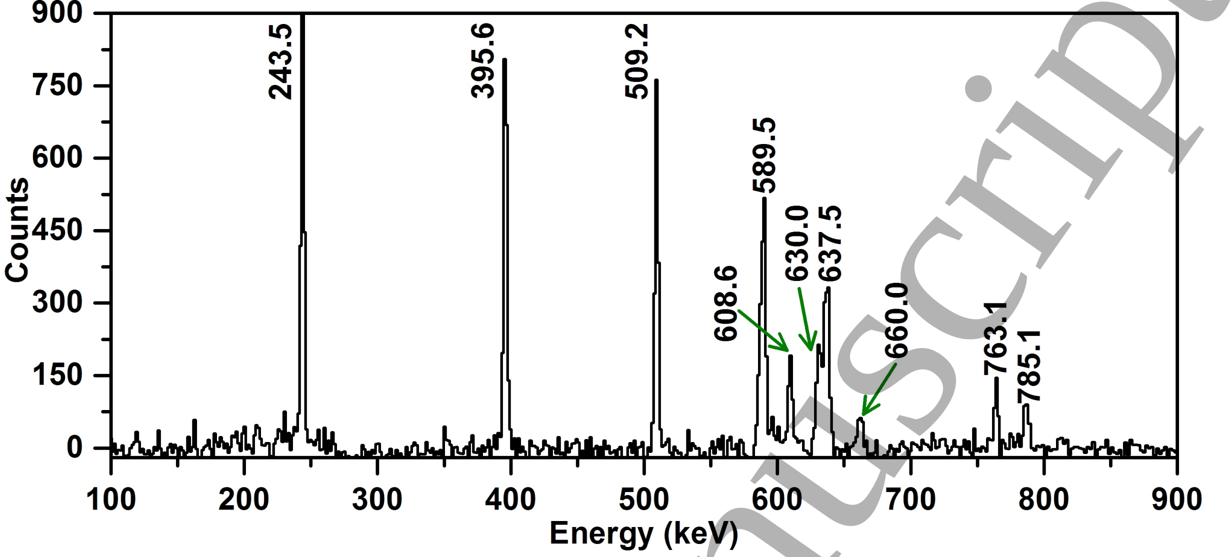

Figure 20. Population of states with spin value ranging from 12^+ to 18^+ of Band-10 are shown with the added cube gates of [(637 & 763) + (637 & 609)+ (637 & 630)+ (763 & 609)+ (763 & 630)+ (763 & 660)+ (609 & 630) + (609 & 660)+ (630 & 660)+ (587 & 785)+ (587 & 630)+ (785 & 630)+ (785 & 660) in keV]. All the γ-rays related to the de-excitation of this band are marked with their energies and the in-band transitions are marked with green arrows.

The presence of Band-10 has been confirmed (c.f. figure 20). It has been observed in the previous work [8]. The spin-parity identification is based on the R(θ) value of the 763 keV transition, connecting this band to the 10^+ level of Band-1. The latter was measured in the present work and confirms $I^\pi=12^+$ identification of the lowest level of Band-10.

6. Discussion

The level structure of ^{160}Yb, observed in the present work, consist of several bands with strongly varying numbers of detected transitions. The highest observed spins are: $I^\pi = (30^+)$ corresponding to Band-1, which manifests the double back-bending and $I^\pi = (30)^-$ corresponding to Band-3.

6.1. Positive-parity bands

Combination of the experimental information at hand with the results of the total energy calculations using standard realistic nuclear mean-field approach confirms certain facts established long time ago in [6, 7, 8], and in particular the nature of the first and of the second back-bending in the yrast line as due to the alignment of the angular momenta of the pairs of $\nu\, i_{13/2}$ and $\pi\, h_{11/2}$ orbitals, the latter conclusion established about 30 years back in [15] using the same modelling principles as the ones used here.

The presence of the hypothetical positive parity Band-9 is confirmed only between 2365.1 keV and 4474.9 keV levels. However, assignment of spins and parities to this band was not possible with the statistics gathered in the present experiment. The population of this band is the weakest among all the observed bands. Existence of the 2_3^+ level at 1292 keV was observed only via β-decay, cf. [42]. The existence of a connection from Band-9 to this level was reported in [5], but could not be confirmed in the present work. Hence, the possibility of interpreting this band as the β-band could not be investigated in the present work.

The structural properties of the positive parity bands are illustrated in figure 21 in the form of comparison of the standard angular momentum alignment plots (the Harris formula parameters used here are taken the same as in [7, 8] to facilitate the comparison with the early references). Illustration reveals certain characteristic similarities and differences in the alignment properties of the positive parity bands shown, in particular the similarities between Band-1 and Band-8.

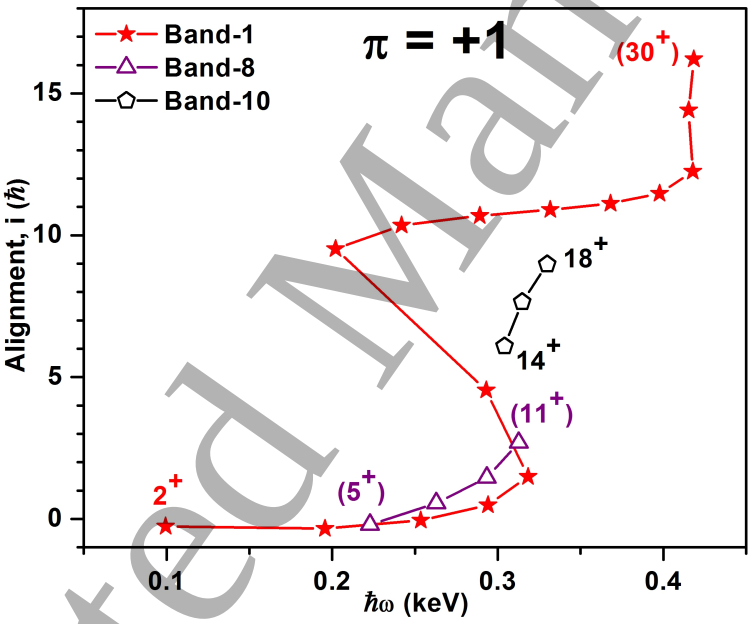

Figure 21. The relative angular momentum alignment for the positive-parity bands in ^{160}Yb, as observed in the present work.

6.2. Negative parity-bands

The spin-parity assignment of 3^- to the 1256 keV level in Band-7 has been confirmed from the E1 nature of the 617 keV transition, thereby confirming that this band has negative parity.

The comparison of the negative parity band properties is illustrated in figure 22 in the form of the angular momentum alignment plots, analogous to the preceding one. The negative-parity signature-partner Band-3 and Band-4, have been argued to originate from a two-quasiparticle neutron excitation of the ground-state configuration [7] and, characteristically, it undergoes a crossing at relatively high frequencies close the the ones of the second (proton) back-bending in the yrast line.

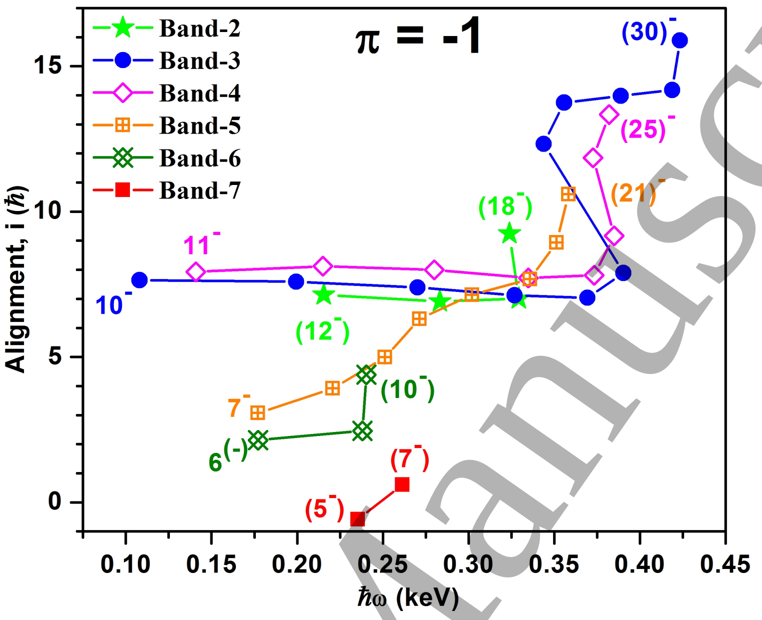

Figure 22. Similar to the preceding one but for the negative-parity bands. The band-crossing in the case of the Band-3 and Band-4 gives rise to the back-bending mechanism at the frequencies close to the second back-bending frequencies in the yrast line.

As it can be seen from the figure, Band-2 manifests the angular momentum alignment features which resemble those in Band-3 and Band-4. At the same time the properties of Band-5, Band-6 and Band-7 are clearly distinct from the remaining bands shown in the figure, even though the small numbers of detected transitions in the sequences 6 and 7 and the related uncertainties make conclusions uncertain in these two cases.

Let us return to the issue of a different structural origin of Band-5 and Band-6 as compared to that of Band-3 and Band-4. Although the low lying 5^- level of Band-5 appears to be similar to the one shown for ^{220}Th by Reviol et al. [47], or in the octupole bands around N = 90 [48], the present work could not confirm the presence of 3^- level or the connection of the 5^- level to be the appropriate band head of Band-5. So, the structure of Band-5 could not be confirmed as of a traditionally known rotationally aligned octupole phonon. Also, the intensity ratios of the intra-band γ-transitions from Band-5 and comparison with a number of odd-spin negative-parity bands in neighbouring nuclei with Z and N close to 70 and 90, respectively, suggests that Band-5 and Band-6 are *not* signature partners, cf. recent [46]. Instead, as argued in this article, whereas the behaviour of Band-5 is compatible with that of a pear-shape octupole one-phonon vibration band, Band-6 could be its analogue in that the Y_{30}-vibration is replaced by the Y_{32}-vibration. The latter structure can be seen as an analogue of the Y_{22}-quadrupole, so-called γ-bands, with the $K^\pi = 2^+$ characteristics – replaced by the Y_{32}-octupole vibrations characterised by $K^\pi = 2^-$ quantum numbers. Such bands are said to have the triplanar-octupole or 'tetrahedral-vibration' structures.

6.3. Weak intensity transitions and assignment uncertainties

The weakest transition that could be confirmed from the triple coincidence data is the 483 keV transition, connecting Band-3 and Band-4, for which the intensity is lower than 0.1% of the $2^+_1 \rightarrow 0^+_1$ transition (the lowest intensity which could be measured in the present work). However, many of the transitions reported in [4, 5] could not be confirmed even with the present selective power of the INGA array. The limiting values of the intensities and the corresponding branching ratios have been estimated from the obtained data.

The non-observation of bands interpreted in [5] as β- and γ-bands might be related to the fact that with the heavy ion reactions it is difficult to populate the low spin states of such non-yrast structures as nearly all of the band-feeding comes from the top of the band with almost no direct side-feeding for the low spin states. Moreover, in the case of a β-, or γ-bands which have similar B(E2) values for both in-band and out-of-band transitions, the later almost double in terms of the transition energy compared to the in-band transitions, the intensities of the in-band transitions are only a few per cent, compared to the out of band transitions. Hence, even if Band-9 could have a connection with the (0^+_2), 1086.1 keV or 2^+_3, 1292 keV levels, the in-band decay of this band below the 2789.9 keV level is very difficult to be traced from triple-coincidence statistics in the present experiment. Unfortunately, the double-coincidence data could not be used because of the presence of multiplets for most of the γ-energies at the bottom of this band. This observation is calling for a new experiment of high statistics feeding preferentially the low and medium spin states with high efficiency. However, this could be difficult to achieve since no light particle reactions are available to feed ^{160}Yb at these spins, hence, the feeding is from top of the band with a large loss of flux at each level because of the unfavourable branching ratios for the in-band vs. out-of-band transitions.

7. Summary and Conclusions

Low and moderately high-spin states in the nucleus ^{160}Yb have been studied using the ^{148}Sm(^{16}O, 4n)^{160}Yb reaction at E_{beam}=90 MeV. Our original choice of this particular nucleus was dictated by the earlier theory predictions suggesting that $Z = 70$ and $N = 90$ are what is referred to as tetrahedral-symmetry magic-numbers. It was encouraged by the attempts by other authors in trying to establish the signals of the tetrahedral symmetry experimentally. In the present experiment, 6.1×10^9 prompt $\gamma - \gamma$ events and, for the first time, 3.5×10^8 prompt $\gamma - \gamma - \gamma$ events were collected by using the INGA array consisting of twenty Compton suppressed clover detectors.

The experimental results concerning the rotational bands presented in this article indicate that with the relatively high sensitivity of the INGA instrument and by using triple-fold coincidences we were not able to confirm the presence of over 70 transitions (many of them crucial for the interpretation purposes) reported in other publications using the double-coincidence analysis only. Detailed presentation of this spectroscopic information has been illustrated and discussed.

We addressed the criteria necessary in establishing whether the signs of the tetrahedral symmetry are present in our data (or not). For this purpose we employed the information from articles published earlier. We formulated and applied synthetic summaries of the two types of arguments. The first one involves the so-called 'historical criteria' based on the conjecture of significant symmetry breaking and weak electromagnetic transitions still present. The other, most recent one is based on the group theory and microscopic Hartree-Fock-Gogny calculations with particle number, parity and angular momentum projections and was formulated in [23, 24] and [3].

In our opinion none of the bands observed in the present experiment satisfies any criteria of compatibility with the presence of the tetrahedral symmetry in this nucleus.

Since consistent predictions by various authors using various methods point repeatedly to the presence of the tetrahedral symmetry in subatomic physics, we believe, we deal not so much with the question of: *Whether such a symmetry exists in nuclei?* – but rather – *How to populate the corresponding states and unambiguously detect the signals of presence of such a symmetry?*

The most promising evolution in this respect will very likely involve a combination of two complementary approaches. Given the fact that at the exact symmetry limit one should expect neither E2 nor E1 transitions involving the members of the tetrahedral bands [cf. eq. (4) and figure 6], one should envisage employing the modern mass spectrometry techniques, cf. [49] and references therein. A very important complementary approach should involve high-resolution γ multi-detection systems to be able to detect the presence of very weak (in this article referred to as residual) quadrupole and dipole moments resulting from the symmetry breaking via zero-point oscillations, the presence of extra particles (or holes) in the doubly-magic tetrahedral-symmetry configurations and symmetry breaking Coriolis effects accompanying an increase in rotational angular momentum.

8. Acknowledgements

The authors gratefully acknowledge the effort of the staff and operators of TIFR pelletron for providing stable good-quality beam. The efforts of Dr. S K Das, Dr. D Banerjee and Mr. R K Chatterjee for preparing the good quality electro-deposited targets is acknowledged. The valuable suggestions received from Dr. S K Basu and Dr. S K Das during experiment are gratefully acknowledged. A Saha acknowledges the UGC JRF/SRF fellowship (ref. No:17-06/2012(i)EU-V) in support of the present work. The authors acknowledge the efforts and support of the INGA collaboration for making the experiment successful. One of the authors (A Chakraborty) would like to acknowledge the financial support from UGC-DAE Consortium for Scientific Research, Kolkata towards his participation at the concerned experiment.

This work was partially supported and by the Polish National Science Centre under Contracts No. 2016/21/B/ST2/01227 and No. 2013/08/M/ST2/00257 (LEA COPIGAL) and by the French-Polish COPIN collaboration, projects No. 04-113 and No. 05-119.

9. References

[1] Dudek J, Góźdź A, Schunck N and Miśkiewicz M 2002 *Phys. Rev. Lett.* **88** 252502

[2] Dudek J, Curien D, Dubray N, Dobaczewski J, Pangon V, Olbratowski P and Schunck N 2006 *Phys. Rev. Lett.* **97** 072501; cf. also:
Dudek J, Góźdź A, Mazurek K and Molique H 2010 *J. Phys. G: Nucl. Part. Phys.* **37** 064032

[3] Dudek J, Curien D, Dedes I, Mazurek K, Tagami S, Shimizu Y R, and Bhattacharjee T 2018 *Phys. Rev.* C **97** 021302(R)

[4] Bark R A, Sharpey-Schafer J F, Maliage S M, Madiba T E, Komati F S, Lawrie E A, Lawrie J J, Lindsay R, Maine P, Mullins S M, Murray S H T, Ncapayi N J, Ramashidza T M, Smit F D and Vymers P 2010 *Phys. Rev. Lett.* **104** 022501

[5] Bark R A, Lipoglavsek M, Maliage S M, Ntshangase S S and Shevchenko A 2005 *J. Phys. G* **31** S1747

[6] Byrski T, Beck F A, Merdinger J C, Nourreddine A, Cranmer-Gordon H W, Elenkov D V, Forsyth P D, Howe D, Riley M A, Sharpey-Schafer J F, Simpson J, Dudek J and Nazarewicz W 1987 *Nucl. Phys. A* **474** 193

[7] Riedinger L L 1980 *Nucl. Phys. A* **347** 141

[8] Riedinger L L, Andersen O, Frauendorf S, Garrett J D, Gaardhoje J J, Hagemann G B, Herskind B, Makovetzky Y V, Waddington J C, Guttormsen M and Tjøm P O 1980 *Phys. Rev. Lett.* **44** 568

[9] Garrett C, Rastikerdar S, Gelletly W and Warner D D 1982 *Phys. Lett. B* **118** 292

[10] Auer H, Fernandez-Niello J, Puchta H and Riess F 1984 *Z. Phys. A* **318** 323

[11] Fewell M P, Johnson N R, McGowan F K, Hattula J S, Lee I Y, Baktash C, Schutz Y, Wells J C, Riedinger L L, Guidry M W, and Pancholi S C 1985 *Phys. Rev. C* **31** 1057

[12] Fewell M P, Johnson N R, McGowan F K, Hattula J S, Lee I Y, Baktash C, Schutz Y, Wells J C, Riedinger L L, Guidry M W, and Pancholi S C 1988 *Phys. Rev. C* **37** 101

[13] Johnson N. R. , McGowan F K, Winchell D F, Baktash C, Garrett J D, Lee I Y, Wells J C, Chaturvedi L, Gao W B, Ma W C, Pilotte S and Yu C H 1996 *Phys. Rev. C* **53** 671

[14] Aguilar A, Campbell D B, Chandler K, Pipidis A, Riley M A, Teal C, Simpson J, Hartley D J, Kondev F G, Clark R M, Cromaz M, Fallon P, Lee I Y, Macchiavelli A O and Ragnarsson I 2008 *Phys. Rev. C* **77** 021302(R)

[15] Ćwiok S, Nazarewicz W, Dudek J, Skalski J and Szymański Z 1980 *Nucl. Phys. A* **333** 139

[16] The approach referred to as “Universal Parameterization of the ‘deformed’ Woods-Saxon Hamiltonian” has been developed in a series of articles:
Dudek J and Werner T 1978 *J. Phys. G: Nucl. Phys.* **4** 1543,
Dudek J, Majhofer A, Skalski J, Werner T, Cwiok S and Nazarewicz W 1979 *J. Phys. G: Nucl. Phys.* **5** 1359 ,
Dudek J, Nazarewicz W and Werner T 1980 *Nucl. Phys. A* **341** 253,
Dudek J, Szymański Z and Werner T 1981 *Phys. Rew. C* **23** 920, and has been summarized in Ćwiok S, Dudek J, Nazarewicz W, Skalski J and Werner T 1987 *Comp. Phys. Comm.* **46** 379

[17] Beck F A, Bożek E, Byrski T, Gehringer C, Merdinger J C, Schutz Y, Styczeń J and Vivien J P 1979 *Phys. Rev. Lett.* **42** 493

[18] Bengtsson R and Frauendorf S 1979 *Nucl. Phys. A* **314** 27 and *Nucl. Phys. A* **327** 139

[19] Ćwiok S, Dudek J and Szymański Z 1978 *Phys. Lett. B* **76** 263

[20] Werner T and Dudek J 1992 *At. Data Nucl. Data Tables* **50** 179

[21] Schunck N, Dudek J and Frauendorf S 2005 *Acta Phys. Polon. B* **36** 1071

[22] Zberecki K, Heenen P H and Magierski P 2009 *Phys. Rev. C* **79** 014319

[23] Tagami S, Shimizu Y R and Dudek J 2013 *Phys. Rev. C* **87** 054306

[24] Tagami S, Shimizu Y R and Dudek J 2015 *J. Phys. G* **42** 015106

[25] Dudek J, Dobaczewski J, Dubray N, Góźdź A, Pangon V and Schunck N 2007 *Int. J. Mod. Phys. E* **16** 516

[26] Krappe H J, Nix J R and Sierk A J 1979 *Phys. Rev. C* **20** 992

[27] Nazarewicz W, Olanders P and Ragnarsson I, Dudek J, Leander G A, Möller P and Ruchowska E 1984 *Nucl. Phys. A* **429** 269

[28] Nazarewicz W, Olanders P, Ragnarsson I, Dudek J and Leander G A 1984 *Phys. Rev. Lett.* **52** 1272

[29] Leander G A, Nazarewicz W, Olanders P, Ragnarsson I and Dudek J 1985 *Phys. Lett. B* **152** 284

[30] Nazarewicz W, Leander G and Dudek J 1987 *Nucl. Phys. A* **467** 437

[31] Dudek J, Curien D, Góźdź A, Shimizu Y R and Tagami S 2013 *Acta Phys. Polon. B* **44** 305

[32] Jentschel M, Urban W, Krempel J, Tonev D, Dudek J, Curien D, Lauss B, de Angelis G and Petkov P 2010 *Phys. Rev. Lett.* **104** 222502

[33] Palit R, Saha S, Sethi J, Trivedi T, Sharma S, Naidu B S, Jadhav S, Donthi R, Chavan P B, Tan H, Hennig W 2012 *Nucl. Instr. & Meth. A* **680** 90

[34] Radford D C 1995 *Nucl. Instr. & Meth. A* **361** 297

[35] Bhowmik R K 2017 *priv. comm.*

[36] Krämer-Flecken A, Morek T, Lieder R M, Gast W, Hebbinghaus G, Jäger H M and Urban W 1989 *Nucl. Instr. & Meth. A* **275** 333

[37] Bhattacharjee T, Chanda S, Bhattacharyya S, Kumar Basu S, Bhowmik R K, Muralithar S, Singh R P, Pattabiraman N S, Ghugre S S, Datta Pramanik U, Bhattacharya S 2005 *Nucl. Phys. A* **750** 199

[38] Droste Ch, Rohoziński S G, Starosta K, Morek T, Srebrny J and Magierski P 1996 *Nucl. Instr. & Meth. A* **378** 518

[39] Starosta K, Morek T, Droste Ch, Rohoziński S G, Srebrny J, Wierzchucka A, Bergstrom M, Herskind B, Melby E, Czosnyka T, Napiorkowski P J 1999 *Nucl. Instr. & Meth. A* **423** 16

[40] Jones P M, Wei L, Beck F A, Butler P A, Byrski T, Duchêne G, de France G, Hannachi F, Jones G D and Kharraja B 1995 *Nucl. Instr. & Meth. A* **362** 556

[41] Bhattacharjee T, Chanda S, Mukherjee A, Bhattacharyya S, Kumar Basu S, Ghugre S S, Dutta Pramanik U, Singh R P, Muralithar S, Madhavan N, Das J J and Bhowmik R K 2008 *Phys. Rev. C* **78** 024304

[42] Reich C W 2005 *Nucl. Data Sheets* **105** 557

[43] Experimental Unevaluated Nuclear Data List Search and Retrieval (XUNDL) http://nndc.bnl.gov/ensdf/ensdf/xundl.jsp, last updated 02.02.2018.

[44] Gavron A 1980 *Phys. Rev. C* **21** 230

[45] Campbel D B *PhD thesis, unpublished* http://diginole.lib.fsu.edu/islandora/object/fsu%3A185022

[46] Saha A *et al.* 2018 *Phys. Scr.* **93** 034001

[47] Reviol W, Chiara C. J., Montero M, Sarantites D. G, Pechenaya O. L, Carpenter M. P, Janssens R. V. F, Khoo T. L, Lauritsen T, Lister C. J, Seweryniak D, Zhu S and Frauendorf S. G 2006 *Phys. Rev. C* **74** 044305

[48] G. L. Zimba, Sharpey-Schafer J. F, Jones P, Bvumbi S. P, Masiteng L. P, Majola S. N. T, Dinoko T. S, Lawrie E. A, Lawrie J. J, Negi D, Papka P, Roux D, Shirinda O, Easton J. E and Khumalo N. A 2016 *Phys. Rev. C* **94** 054303

[49] Dudek J, Dedes I, Yang J, Baran A, Curien D, Dickel T, Góźdź A, Rouvel D and Wang H-L 2019 *Acta Phys. Polonica* in print